Determination of the Absolute X-Ray Detection Efficiency of the TAXO SDD for IAXO

Masterthesis

Patrick Bongratz

03684270

Course of studies:

Nuclear, Particle and Astrophysics

at the

Technical University Munich

18.10.2024

Primary Reviewer:	Prof. Dr. Susanne Mertens
Secondary Reviewer:	Dr. Raimund Strauß
Supervisor:	Dr. Christoph Wiesinger

Abstract

Axions are hypothetical particles, proposed to solve the strong CP problem. Furthermore, axions are a potential candidate for dark matter. The International AXion Observatory (IAXO), a fourth-generation helioscope, aims to detect axions produced in the Sun by converting them into X-ray photons in a strong magnetic field. These X-rays are then focused to a high detection efficiency, and low background detector, like the TAXO Silicon Drift Detector (SDD). The goal of this thesis is the determination of the absolute X-ray detection efficiency of this SDD for the IAXO helioscope experiment.

The experiment to measure the detection efficiency of the SDD was conducted at the SOLEIL Synchrotron on the Metrology beamline. The detection efficiency was measured in the energy range of 3 to 35 keV which covers most of the region of interest for IAXO. To this end, a custom SDD holder with integrated cooling has been designed in this work. The measured detection efficiency was found to be close to 100% for energies below 10 keV and decreasing for higher energies. The measured efficiency curve closely follows the theoretical predictions. This confirms the excellent performance of the TAXO SDD for detecting low-energy X-rays, particularly in the range most relevant to solar axions. This work is the first validation of the TAXO SDD's excellent detection efficiency, bringing it closer to incorporation in IAXO and contributing significantly to the ongoing search for axions.

Zusammenfassung

Axionen sind hypothetische Teilchen, die eingeführt wurden, um das starke CP-Problem zu lösen. Darüber hinaus sind Axionen ein potenzieller Kandidat für Dunkle Materie. Das International AXion Observatory (IAXO), ein Helioskop der vierten Generation, zielt darauf ab, Axionen, die in der Sonne erzeugt werden, nachzuweisen, indem sie in einem starken Magnetfeld in Photonen umgewandelt werden. Diese Photonen liegen in dem Energiebereich von Röntgenstrahlen. Die Strahlen werden dann auf einen Detektor mit hoher Detektionseffizienz und niedrigem Hintergrund, wie den TAXO Silicon Drift Detector (SDD), fokussiert. Das Ziel dieser Arbeit ist die Bestimmung der absoluten Detektionseffizienz des SDD für das IAXO-Helioskop.

Das Experiment zur Messung der Detektionseffizienz des SDD wurde am SOLEIL-Synchrotron an der Metrologie Strahllinie durchgeführt. Die Detektionseffizienz wurde im Energiebereich von 3 bis 35 keV gemessen, was den Großteil des für IAXO interessanten Bereichs abdeckt. Zu diesem Zweck wurde in dieser Arbeit ein eigener SDD-Halter mit integrierter Kühlung entworfen. Die gemessene Detektionseffizienz liegt bei Energien unter 10 keV knapp unter 100% und nimmt bei höheren Energien ab. Die gemessene Effizienzkurve ist dabei nahe an den theoretischen Vorhersagen. Dies bestätigt die hervorragende Leistung des TAXO SDD bei der Detektion von niederenergetischen Röntgenstrahlen, insbesondere im für solare Axionen relevanten Bereich. Diese Arbeit stellt den ersten Beweis der exzellenten Detektionseffizienz des TAXO SDD dar und bringt dessen Integration in IAXO einen guten Schritt näher, wodurch ein bedeutender Beitrag zur laufenden Suche nach Axionen geleistet wird.

Contents

Abstract **I**

Zusammenfassung **II**

1 Axions **1**

1.1 Motivation . . . 2

1.1.1 The Strong CP Problem . . . 2

1.1.2 Peccei-Quinn Mechanism . . . 2

1.1.3 Primakoff Effect . . . 4

1.1.4 Axion-like particles . . . 6

1.1.5 Axions as Dark Matter Candidates . . . 6

1.2 Experimental Efforts . . . 8

1.2.1 Haloscopes . . . 9

1.2.2 Light-Shining-through-a-Wall Experiments . . . 10

1.2.3 Helioscopes . . . 11

2 IAXO **13**

2.1 Goals . . . 16

2.2 BabyIAXO . . . 17

2.3 Detector Challenges . . . 20

2.4 Tristan SDD for IAXO . . . 22

2.4.1 Silicon Drift Detectors . . . 22

2.4.2 7-Pixel TAXO SDD . . . 24

3 Efficiency Measurement **26**

3.1 SOLEIL . . . 26

3.1.1 The Synchrotron . . . 26

3.1.2 Metrology Beamline . . . 27

3.2 SDD Holder and Cooling System . . . 31

3.3 Experimental Setup . . . 33

3.3.1 Data Acquisition . . . 33

3.3.2 Data Processing . . . 35

3.4 Measurements . . . 38

4 Data Analysis **43**

4.1 Beam Rate Determination . . . 44

4.2 SDD Rate Determination . . . 49

4.3 Absolute Detection Efficiency of the TAXO SDD . . . 54

4.4 Beam Harmonics . . . 55

5 Conclusion and Outlook **57**

List of Figures **58**

List of Tables **60**

Acronyms **61**

References **62**

1. Axions

The universe is filled with unanswered questions that challenge our understanding of fundamental physics. Among them are the nature of dark matter, the possible existence of sterile neutrinos, and the puzzling matter-antimatter asymmetry. Of these, dark matter stands out as a long-sought-after mystery. The effects of the presence of dark matter are observable even in the rotational curves of galaxies like the Milky Way, where visible matter alone cannot explain the observed motion. Despite barely interacting with ordinary matter, dark matter is estimated to make up roughly 85% of the universe's gravitating mass.

A promising solution to this mystery is the existence of axions. First proposed in the context of quantum chromodynamics (QCD) to solve the strong CP problem, axions are hypothetical particles that could also explain dark matter. These weakly interacting particles, when found to exist, could account for the universe's missing mass and solve several other fundamental questions in astrophysics and cosmology.

For this reason, the search for axions is an essential part of modern experimental physics. The future IAXO helioscope experiment is one of the main representatives in this field. Therefore, the objective of this thesis is the determination of the absolute detection efficiency of a possible IAXO detector.

The properties and motivation for the existence of axions are elaborated in Chapter 1.1. The experimental efforts in the search for axions are discussed in detail in Chapter 1.2. This includes the difference in the individual experimental approaches.

1.1. Motivation

1.1.1. The Strong CP Problem

The combination of the symmetries of charge conjunction $\mathcal{C}$, parity $\mathcal{P}$, and time reversal $\mathcal{T}$ must always be conserved. However, the combined symmetry of charge conjugation and parity ($\mathcal{CP}$) can be violated, which was first observed for the weak interaction in 1964 for the decay of neutral kaons ($K \rightarrow \pi\pi$) [1]. In quantum chromodynamics (QCD), the quantum field theory that describes the strong interaction between quarks and gluons [2], the $\mathcal{CP}$ symmetry seems to be violated. This is due to a term, specifically from the QCD Lagrangian, depending on the non-zero QCD vacuum angle θ [3], as seen in equation 1.

$$\mathcal{L}_\theta = \theta \frac{\alpha_s}{8\pi} G^a_{\mu\nu} \widetilde{G}^{\mu\nu}_a \tag{1}$$

Here, α_s is the QCD-equivalent of the fine-structure constant, and $G^a_{\mu\nu}$ and $\widetilde{G}^{\mu\nu}_a$ are the colour field strength tensor and its dual, respectively [4]. From theoretical considerations, the vacuum angle θ can be between 0 and 2π, and a non-zero value implies a $\mathcal{CP}$ violation [5]. Considering equation 2, $\theta > 0$ also results directly in a measurable electric dipole moment (EDM) for the neutron d_n [6].

$$d_n = 3.6 \times 10^{-16} \theta \ e \ \mathrm{cm} \tag{2}$$

Not only was this not measured so far, but the upper limit for the neutron EDM is currently at [7]:

$$|d_n| < 1.8 \times 10^{-26} \ e \ \mathrm{cm} \tag{3}$$

With equation 2, this results in the upper limit for the QCD vacuum angle as $\theta < 10^{-10}$. This tiny value as the upper limit means that the vacuum angle θ is basically at zero and, therefore, violates the CP symmetry. There is no theory-motivated reason for this value to be zero. This fine-tuning problem is known as the *Strong $\mathcal{CP}$-Problem.*

Several theories have been proposed as potential solutions to this problem. One promising approach is the Peccei-Quinn mechanism, which will be elaborated on in the following section.

1.1.2. Peccei-Quinn Mechanism

Different solutions to the strong CP problem have been proposed over the years. While many theories, like one quark being massless, have now been excluded, a promising theory is the Peccei Quin mechanism as a possible solution to the strong

CP problem [8]. It was first formulated by R. D. Peccei and H. R. Quinn in 1977 [9, 10] and is based on a new global chiral $U(1)$ symmetry. It is one of the theoretically and experimentally most investigated solutions to the strong CP problem [11]. The Peccei-Quinn symmetry denoted as $U(1)_{PQ}$ is spontaneously broken at high energy scales f_A.

Here, the θ-parameter is effectively turned into a dynamical variable $\theta \rightarrow \theta\,(t,x)\,\frac{\phi(t,x)}{f_A}$. The QCD Lagrangian term $\mathcal{L}_\theta$ is therefore replaced by $\mathcal{L}_a$ [12]:

$$\mathcal{L}_a = \frac{\alpha_s}{8\pi} G^a_{\mu\nu} \widetilde{G}^{\mu\nu}_a \frac{\phi}{f_A} \tag{4}$$

Here, ϕ is the axion field, and f_A is the decay constant. With this, θ as a dynamical variable allows it to naturally go to zero while minimising ϕ. This would explain the fine-tuning of θ and the absence of CP symmetry breaking in the strong interactions, solving the Strong CP-Problem.

A relevant part of the Peccei-Quinn mechanism is the implication of a new particle corresponding to the oscillations of ϕ. Following the Goldstone theorem, the new particle results from the spontaneously broken global symmetry $U(1)_{PQ}$ and is, therefore, a massless Goldstone boson [13]. Steven Weinberg and Frank Wilczek both realised the possibility of the existence of this new particle independently in 1978 [14, 15], and Wilczek first named it the Axion.
The Axion acquires a mass through QCD mixing with π^0 and other mesons. The mass is given by equation 5. The dependence on the QCD mixing implies that this condition does not hold for energies above the QCD confinement scale, making axions effectively massless in high-energy environments such as the early universe [16].

$$m_A = 5.70\ \mu\text{eV} \left(\frac{10^{12}\ \text{GeV}}{f_A} \right) \tag{5}$$

The axion mass directly depends on f_A, which is not restricted by theory. This leads to a wide range of possible axion masses. The potential for the axion field can be defined as [17]:

$$V(\varphi) = \lambda \left(|\varphi|^2 - \frac{f_A^2}{2} \right)^2 \tag{6}$$

with the complex scalar φ:

$$\varphi = \chi e^{i\phi/f_A} \tag{7}$$

This means that the axion ϕ is effectively a phase of φ. Here, λ is a dimensionless coefficient. At very high energies, where the axion is massless, the corresponding potential takes on a parabolic shape, with its minimum at zero. In a transitional region below the Peccei-Quinn scale but above the QCD scale, the axion acquires a

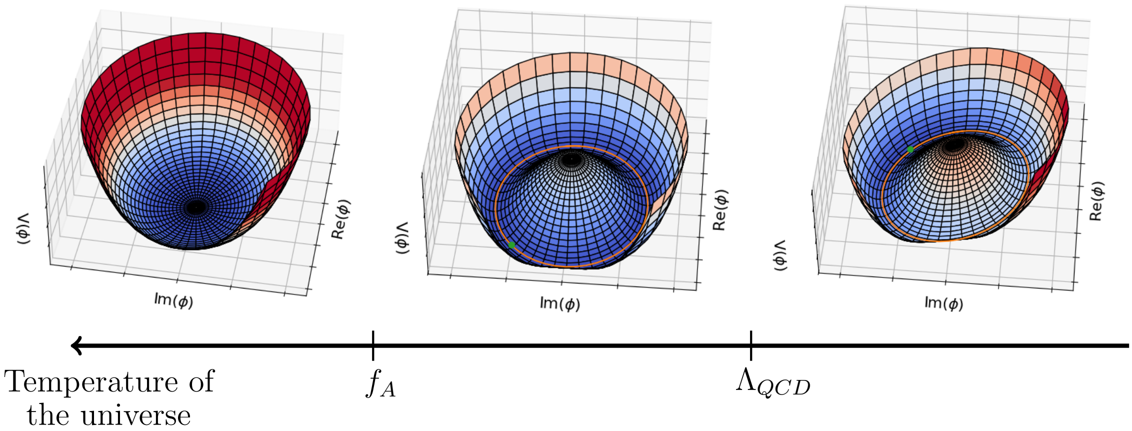

Figure 1: **Illustration of the axion potential**
The complex scalar field ϕ, representing the axion, always takes on the minimum value of its potential $V(\phi)$. At very high temperatures, like in the early universe, the axion potential takes on a parabolic shape, as seen in the left panel. At this stage, the potential minimum is at zero, making the axion massless. When the temperature of the universe decreases below an energy of f_A, the potential takes on a mexican-hat shape. The radius of the bulk is corresponding to f_A. This shifts the vacuum expectation value of ϕ to $<\phi>= f_A/\sqrt{2}$. The phase θ takes on an arbitrary value. This breaks the initial U(1) symmetry and creates a new boson, the axion. This can be seen in the middle panel. When the temperature of the universe drops below the QCD scale of $\Lambda_{QCD} \approx 200$ MeV, the potential starts tilting. This is due to the strong interaction with the gluon field. At this point, ϕ moves toward the single minimum value and starts oscillating around it. This realignment is referred to as the vacuum realignment mechanism. Due to this oscillation, the vacuum expectation value of the potential takes on a non-zero energy, giving the axion a mass. Adapted from [8]

non-zero vacuum expectation value. At this energy, the axion is still massless, but the potential takes on a "Mexican-hat" shape. Below the QCD scale the potential tilts, leading to a single fixed mass value for the Axion [17]. This transition is illustrated in figure 1.

1.1.3. Primakoff Effect

To allow the production, detection, and integration of axions into the Standard Model (SM) of particle physics, they must couple to photons or other forms of ordinary matter. One of the most common coupling mechanisms is the Primakoff effect. This effect was first introduced by Henry Primakoff in 1951 allowing the coupling of the pseudo-scalar field of a π^0-mesons to a photon in the presence of the electromagnetic field of a nucleus mediated through a virtual photon [18].

This can be applied to the axion, as first established by P. Sikivie in 1983 [19], coupling it to a photon within a strong magnetic field. The process works in both directions. This makes it an axion production mechanism, i.e. in the plasma at the centre of a star [20], and a possible detection principle. Figure 2 depicts the

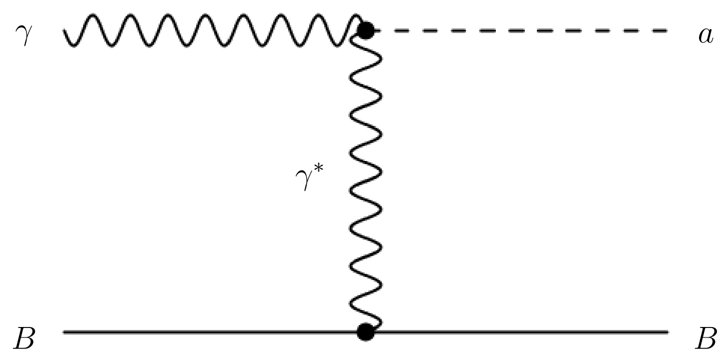

Figure 2: **Feynman diagram of the Primakoff effect**
In this Feynman diagram the conversion of a photon γ into an axion a (and vice versa) is illustrated. The coupling is happening in the presence of an external magnetic field B, mediated by a virtual photon γ^*.

Feynman diagram of this bi-directional process.

The interaction term of axion-to-photon coupling is given by equation 8.

$$\mathcal{L} = -g_{a\gamma}\phi\mathbf{E}\cdot\mathbf{B} \tag{8}$$

Here, $g_{a\gamma}$ is the axion-to-photon coupling strength, ϕ is the axion field, and $(\mathbf{E}\cdot\mathbf{B})$ is the electromagnetic field [21]. The coupling constant $g_{a\gamma}$ can be defined as

$$g_{a\gamma} = \frac{\alpha}{2\pi}\frac{1}{f_A}\left(\frac{E}{N} - C\right). \tag{9}$$

The ratio $\frac{E}{N}$ is a model-dependent constant. The factor C is a constant that includes the ratio of different quark masses. The coupling strength is inversely proportional to the unfixed decay constant f_A. The current limit on the axion-to-photon coupling is $g_{a\gamma} < 5.7 \times 10^{-11}\ \mathrm{GeV}^{-1}$ for an axion mass $m_a \lesssim 0.02\,\mathrm{eV}$ [22].

The model-dependent constant for the two main classes of axions is $\frac{E}{N} = 0$ for Kim-Shifman-Vainshtein-Zakharov (KSVZ) axions and $\frac{E}{N} = 8/3$ for Dine-Fischler-Srednicki-Zhitnitskii (DFSZ) axions. Both theories are extensions of the Standard Model. The main difference is the factor 3 weaker axion coupling for the DFSZ axions. [23]

Although the axion's strongest coupling is to photons, it can also couple to other SM particles. The second most popular axion coupling is to Dirac fermions, more specifically, electrons. For electrons, the coupling is given by equation 10. [24]

$$\mathcal{L}_{ae} = -g_{ae}\frac{\partial_\mu\phi}{2m_e}\bar{\psi}\gamma^5\gamma^\mu\psi \tag{10}$$

Here, ψ is the Dirac spinor, and g_{ae} is a dimensionless coupling strength. Axions generated through electron couplings can originate from processes such as axio-recombination, bremsstrahlung, or Compton scattering. Therefore, they are often called "ABC axions" [25]. The limit for axion-to-electron coupling is $|g_{ae}| < 3\times10^{-11}$ for $m_a \lesssim 0.01\,\mathrm{eV}$ [26].

Additional axion interactions have been proposed, for instance, in supernovae, where axions couple directly to nuclei [27]. However, such axions are not considered significant for most axion experiments or cosmological models.

1.1.4. Axion-like particles

In multiple extensions of the Standard Model, like String Theories, particles sharing several properties with the QCD axion are postulated [28]. The main difference between these particles and the QCD axion is that they do not solve the strong CP problem. They can also interact, however, with SM particles via the Primakoff effect. This similarity leads to such particles being referred to as axion-like particles, or ALPs. The axion and ALPs are considered a part of Weakly Interacting Slim Particles (WISPs), a possible new family of particles [29].

The coupling of ALPs, as well as axions, depends on the decay constant f_A. ALPs, however, do not necessarily get their mass from QCD effects like the QCD axion. Instead, they receive mass from other dynamics, explicitly breaking their global U(1) symmetry. This allows for a wide range of possible particles to exist [30]. The similarity in interactions allows most experiments based on the Primakoff effect to search for axions and ALPs. For this reason, the names "axion" and "ALP" are commonly used interchangeably. This is why, in the following, the name "axion" is representative of both, while "QCD axion" is used when explicitly referring to the CP problem-solving axion.

1.1.5. Axions as Dark Matter Candidates

The axion results from a solution to the strong CP problem. Today, the interest in finding the axion goes way further since it is also a promising dark matter (DM) candidate. The puzzle about the dark matter content in the universe is one of the big mysteries of the present. It describes the discrepancy between the amount of matter observed by cosmological measurements and the amount required to account for various gravitational phenomena.

This mismatch can be observed, for example, by measuring a spiral galaxy's rotational curve with a radio telescope and comparing it to theoretical calculations based on the visible matter in the galaxy [31]. The observed rotation speed in the outer part of the galaxy is considerably faster than expected from the calculation. This implies the presence of additional matter, which interacts only via the gravitational force, thus appearing "dark". Cosmological observations indicate that about 80% of all gravitating matter in the universe exists in the form of dark matter [32].

There are several potential solutions to the dark matter problem, most of which propose the existence of new particles. The most promising theories include sterile neutrinos, WIMPs (Weakly Interacting Massive Particles), or axions, all of which interact weakly with ordinary matter. Cosmological observations favour cold or non-relativistic dark matter, making the axion a viable candidate, as it would be non-thermally produced. The axion density relative to the critical density of the universe is given by

$$\Omega_a \approx \left(\frac{6\mu\mathrm{eV}}{m_a}\right)^{\frac{7}{6}}. \tag{11}$$

An axion mass of $m_a \approx 20\,\mu$eV would correspond to $\Omega_a \approx 0.24$ and could account for the entire dark matter density of the universe [29]. Therefore, the axion, solving two problems at once, is a rather desirable particle for experimental verification.

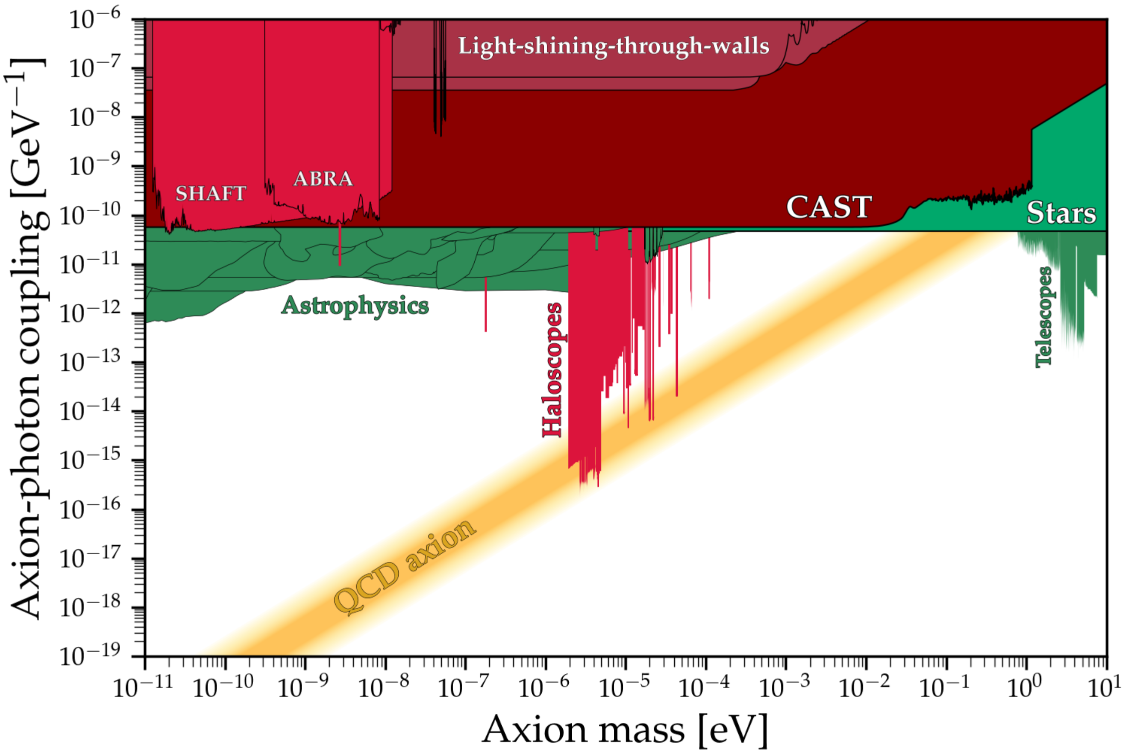

Figure 3: **Axion parameter space exclusions**
The current exclusion limits on axion-photon coupling as a function of the axion mass is shown. A yellow diagonal band indicates the regime for axions that could solve the strong CP problem. The exclusion limits from haloscopes, light-shining-through-a-wall experiments, the latest helioscope CAST, and astrophysical limits are indicated, respectively. Adapted from [33].

1.2. Experimental Efforts

Different experimental approaches have been utilised in the search for the axion. The working principle of most of them relies on the Primakoff effect, resulting in the coupling between axions and photons [30]. This is described by the coupling constant $g_{a\gamma}$, as explained in chapter 1.1.3. The difference in the approaches is mainly where the axions are produced.

Despite numerous experimental efforts, the axion remains elusive. The different experiments progressively test and reduce the parameter space of possible axion detection. This parameter space commonly depicts the $g_{a\gamma}$-m_a-plane, with $g_{a\gamma}$ as the axion-to-photon coupling strength and m_a as the axion mass. Both variables are directly related to the decay constant f_A. The current limits can be seen in figure 3. The region of axions that would solve the Strong CP-Problem can be seen as a diagonal band in this figure.

The three main approaches are based on three corresponding axion origins. The first approach is the search for axions from the dark matter halo around our galaxy. These experiments try to detect the axion within a microwave cavity. The second approach is the concept of Light-Shining-through-a-Wall (LSW) experiments. As the name suggests, these experiments try to detect the axion by shining a strong light source onto a wall with a detector behind it and a strong magnetic field around the structure. Therefore, trying to detect axions, which are created in the laboratory. The third experimental approach for the axion search is the search for solar axions inside an axion-helioscope. In these experiments, axions created in the sun are converted to X-ray photons inside a strong magnetic field and then focused on a high-efficiency, low-background detector. These three experimental approaches in the search for the axion are explained in more detail in the following sections.

1.2.1. Haloscopes

In haloscopes, axions are converted to microwave photons in a strong magnetic field. The frequency of these photons is correlated to the mass of the axion. The microwave photons can be detected in dedicated resonant cavities immersed in a strong magnetic field [34]. Pierre Sikivie, the first person to apply the Primakoff effect to the axion, used this detection principle already in 1983 in the Sikivie experiment [19].

The advantage of haloscope experiments is an unmatched sensitivity, down to 10^{-16} GeV^{-1}. This is possible because every photon frequency correlating to a specific axion mass is probed individually by tuning the cavity to resonate with each frequency. In some haloscopes, the tuning is done by changing the geometry of the cavity by moving so-called tuning rods. When the cavity is tuned to a specific frequency, the tiny photon signal is amplified by ultra-low noise quantum amplifiers.

Despite having an excellent sensitivity, haloscopes have two main disadvantages. The first disadvantage is that the resonant cavity is only tuned for one frequency at a time. Therefore, each specific axion mass must be probed individually. This leads

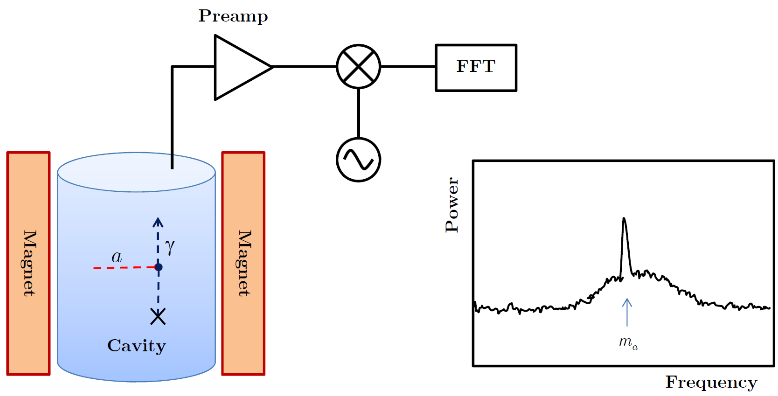

Figure 4: **Working principle of a haloscope**
In haloscopes axions are converted to photons inside a microwave cavity (blue). The strong magnetic field required for the conversion is created with magnets surrounding the cavity (orange). The tiny signal from an axion, visible in the right panel, can be detected through quantum amplification. Adapted from [8].

to haloscopes appearing as narrow streaks in the axion parameter space exclusions. Therefore, only small regions of the parameter space can be probed at a time.

The second disadvantage is that the resonance frequency of the cavity depends on its size. Therefore, the experiment size is directly tied to the axion mass range that can be probed. This is very limited since for large cavities, probing low axion masses, it can be challenging to provide a sufficiently strong magnetic field. Also, for small cavities probing higher axion masses, the detection volume quickly decreases. For this reason, haloscope experiments focus on an axion mass below 10^{-3} eV.

A sketch of the working principle of a haloscope is shown in figure 4. A prominent representative for haloscope experiments, pushing axion exclusion limits, is the Axion Dark Matter EXperiment (ADMX) [35].

1.2.2. Light-Shining-through-a-Wall Experiments

The second main approach used in axion search experiments is Light Shining through a Wall (LSW) experiments. This type of experiment, first proposed in 1983, is based on converting axions into photons, and vice versa, in the presence of a strong external magnetic field [36].

In these experiments, a high-power laser (HPL) emits photons through a strong magnetic field onto a barrier that blocks photons. In the region between the laser and the wall, the photons can be converted to axions via the Primakoff effect. This allows them to pass through the barrier. Behind the barrier is another region immersed in a strong magnetic field, where the axions can recouple through the same effect back to photons. A high-sensitivity detector can then detect these photons [37]. Figure 5 depicts this working principle.

Compared to haloscopes, the advantage of LSW experiments is that they use laboratory-

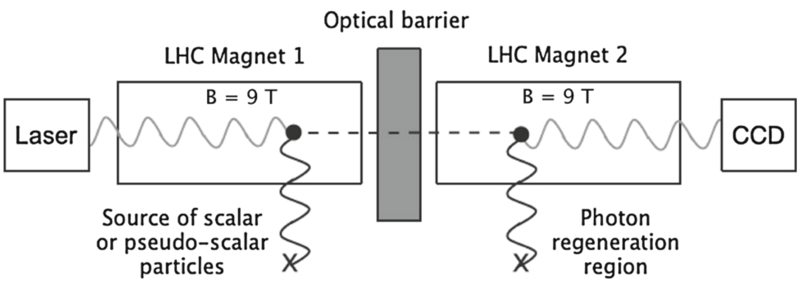

Figure 5: **Working principle of Light-Shining-through-a-Wall (LSW) experiments**
The working principle of LSW experiments on the example of the OSQAR experiment is depicted. Photons from a laser are converted to axions in the strong magnetic field, allowing them to propagate through an optical barrier. Behind the barrier, the axions are reconverted to photons in a second magnetic field and absorbed by a detector in the back. Adapted from [38].

created axions. Creating their own axions in the experiment makes it completely independent from astrophysical models. This allows LSW experiments to independently determine the axion-to-photon coupling strength without relying on an external model of the axion flux. [39]

On the other hand, converting photons to axions and then back to photons requires the Primakoff effect to occur twice. This significantly reduces the sensitivity of LSW experiments. [29] The most prominent LSW experiments are the Any-Light-Particle-Search (ALPS) [40] and the Optical Search for QED Vacuum Birefringence, Axions, and Photon Regeneration (OSQAR) [41]. The successor to ALPS, ALPSII, is currently under construction. [39]

1.2.3. Helioscopes

The third main type of axion experiment is the helioscope. Similar to LSW experiments, helioscopes try to detect a directional flux of axions. The difference is the axion source. Helioscopes are designed to detect axions originating from the sun.

The motivation for using solar axions is having excellent axion production conditions in the solar centre. The two main factors for axion production via the Primakoff effect are a high photon flux and a strong magnetic field. Both conditions are satisfied in the plasma of the sun's core. The expected energy spectrum resulting from this production mechanism is shown as a black graph in figure 6.

An advantage of helioscopes is that they are not exclusively sensitive to $g_{a\gamma}$ couplings but also other axion production mechanisms, like g_{ae} coupling for producing ABC axions. The expected ABC axion flux is shown as a grey graph in figure 6. The axion can propagate freely from the sun's plasma to the Earth since it interacts only weakly.

Axion helioscope experiments can be divided into two parts. In the first part, the axions enter the helioscope and convert to X-ray photons inside a strong magnetic field created by superconducting magnets. Due to the heavy magnets and necessary cooling system, this is the most massive part of the experiment. The second part is the telescope that is mounted on the back end of the magnet bore. This telescope is comprised of X-ray focusing optics and a high-sensitivity detector. The optics focus the created X-ray photons from the magnet bores down to a small focal point. The X-ray detector requires a high detection efficiency and a low background. Additionally, the whole structure needs to be mounted on a movable platform. This is necessary to track the sun's position and keep the solar axion flux parallel to the optics. A sketch of a helioscope's structure is depicted in figure 7.

The CERN Axion Solar Telescope (CAST) [42] was the most recent axion helioscope experiment. The limit of $g_{a\gamma} = 8.8 \times 10^{-11}\text{GeV}^{-1}$ [22] is the most stringent limit set

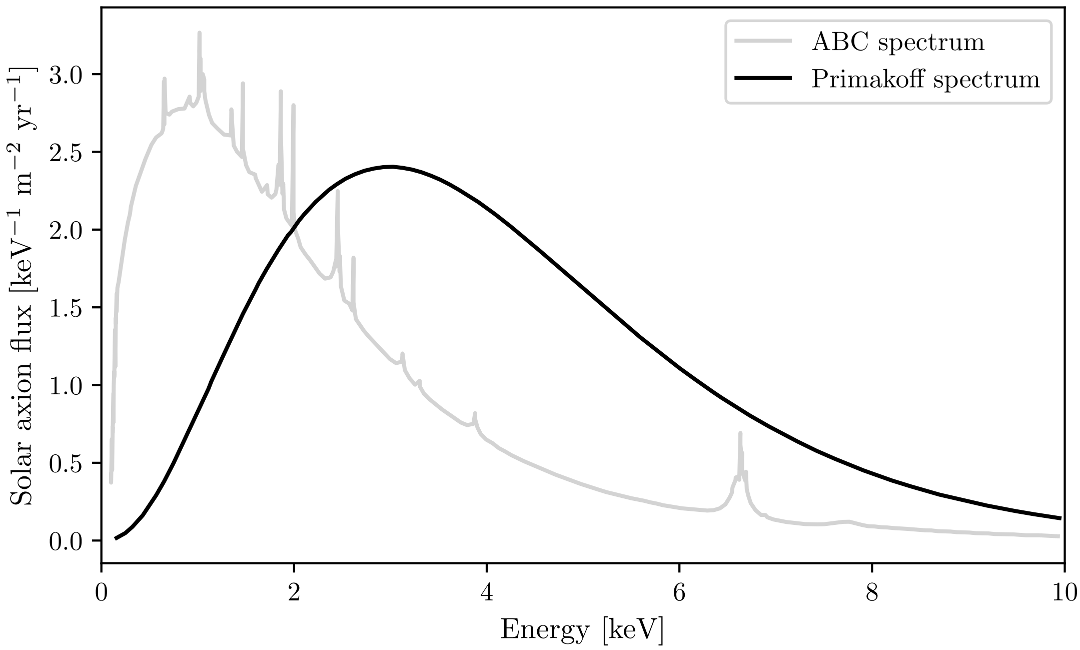

Figure 6: **Solar axion flux spectra**
The axion flux for different axion production mechanisms is shown. The axion production via the Primakoff effect with $g_{a\gamma}$ coupling is shown in black. The expected ABC axion flux through g_{ae} coupling is shown in grey. Data taken from [8].

by a current helioscope. The successor of CAST is aiming to push those limits and is currently under development.

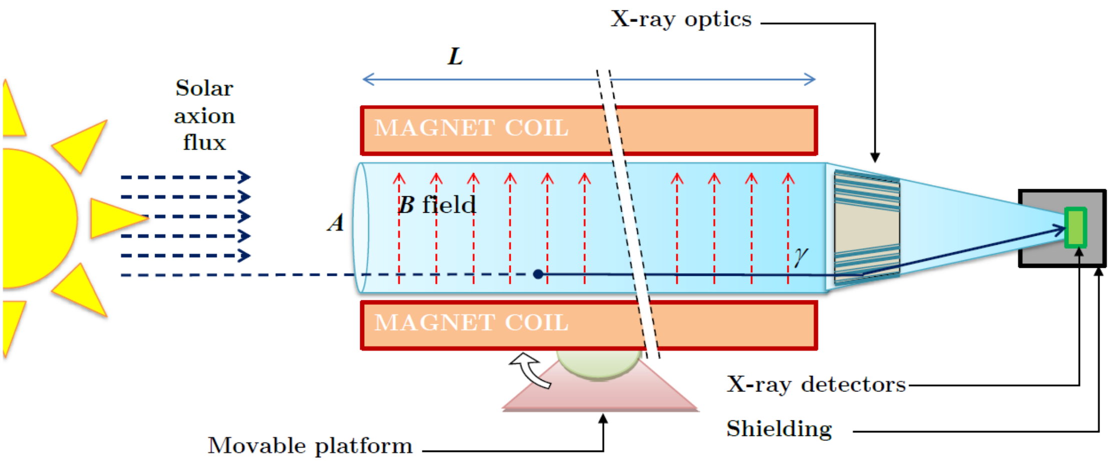

Figure 7: **Structure of an axion helioscope**
Solar axions, produced in the sun's core, enter the bore. This bore is equipped with strong superconducting magnets, where the axions are converted to X-ray photons. Specialised optics then focus the photons to a high-efficiency, low-background detector. Adapted from [8]

2. IAXO

The successful operation of the concluded CAST helioscope experiment [22] is the motivation for building a further improved successor axion helioscope. The advantages of a helioscope compared to other experimental approaches are described in chapter 1.2. The **International AXion Observatory** (**IAXO**) will be this successor [43]. IAXO is a next-generation axion helioscope currently under development. It will push the CAST sensitivity levels of the axion parameter space by more than one order of magnitude, probing new areas of the QCD band. This will be achieved by applying cutting-edge technology and using custom-developed components for the composition of IAXO. The proposed design for the future IAXO helioscope is shown in figure 8.

The IAXO helioscope will include eight racetrack coil magnets that are 25 m long and 1 m wide. These eight superconducting magnets are arranged in a circle with a diameter of 5.2 m. The magnet system will generate a peak magnetic field of 5.4 T. Between each pair of magnets is a bore where axions couple with the magnetic field to produce X-ray photons. This configuration can be seen in figure 9. To

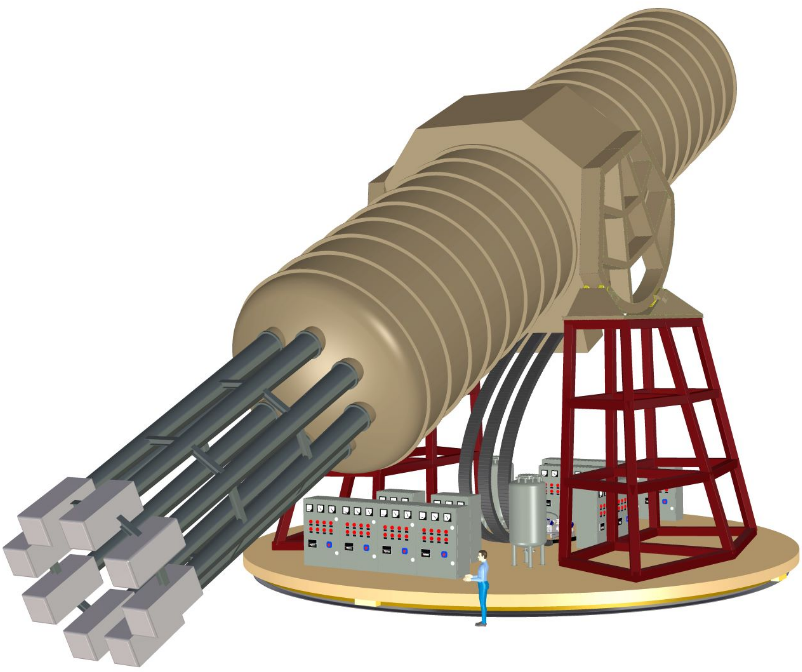

Figure 8: **Conceptual IAXO design**
The proposed structure includes a 25 m long magnet system (shown in beige) containing eight racetrack coils, where solar axions are converted into X-ray photons. At the end of each magnet, a system of X-ray focusing optics (depicted as dark grey tubes) directs the X-rays onto a high-efficiency, low-background detector. To further reduce the background, the detectors are enclosed in specialised shielding, represented by light grey blocks in the figure. The whole structure is mounted on a movable platform to allow the helioscope to track the sun. Adapted from [44].

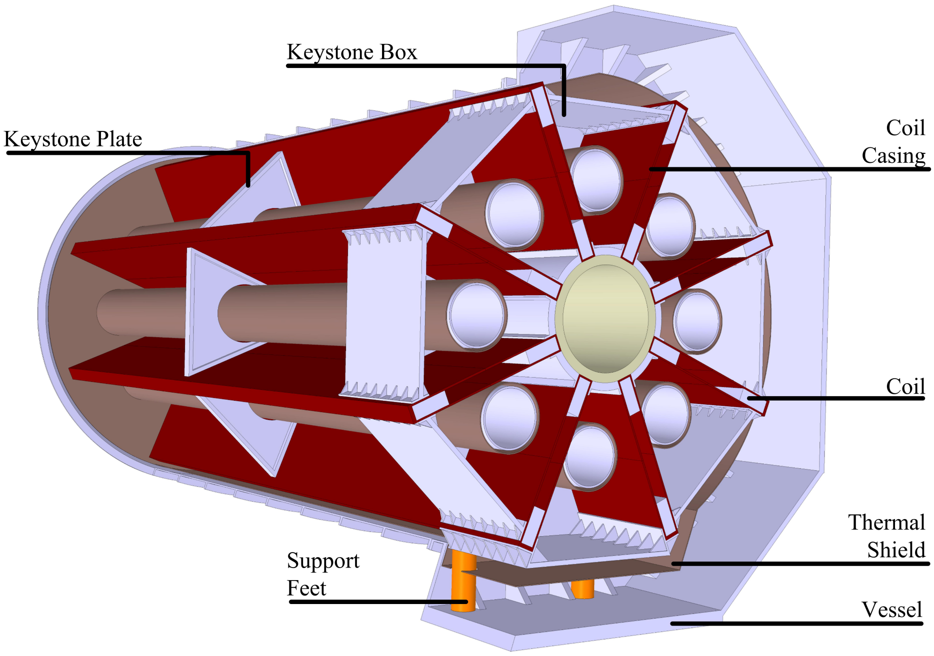

Figure 9: **Conceptual design of the IAXO magnet bore system**
The rectangular racetrack coils are depicted in red with the bores for the axion-to-photon conversion between them. The thermal shielding and structural support components are shown in white. Adapted from [43].

operate the superconducting magnets, a cold mass of 130 tons needs to be cooled to a temperature of approximately 4.5 K. This is achieved by a cryogenic system enveloping the magnets. The cooling is based on sub-cooled liquid helium circulating at super-critical pressure.

The X-rays created by axions inside the bores are focused by X-ray optics at the end of each bore onto a detector system. Eight custom-developed focusing optics, one for each bore, are included in the IAXO design. The X-ray optics focus the X-rays from the 60 cm diameter of the bores down to an area of $\sim 0.2\text{cm}^2$. This minimisation of the detection area leads to a better background performance. The optics are part of the telescope for the helioscope.

One of the key components of IAXO is the high-efficiency, low-background detector at the focal point of the telescope. As a rare event search experiment, with only a couple of events per year [8], a high detection efficiency plays an especially important role in the detector's choice. To develop a detector suitable for these challenging conditions, an IAXO subgroup focuses on the possibility of using silicon drift detectors (SDDs).

One additional challenge is the holding structure which allows the experiment to follow the sun in elevation and azimuthal angle. This is necessary to keep the incident solar axions parallel to the telescope for up to 12 hours per day. This is a significant improvement compared to CAST, which previously could only track the sun for 3 hours per day, divided between sunrise and sunset. Despite the presence of the 5-meter-long telescopes at one end, the centre of mass, and the mounting point on the moving platform, of the entire structure remains near the middle of the magnet system, owing to the large mass of the magnets and the cryogenic system. [43]

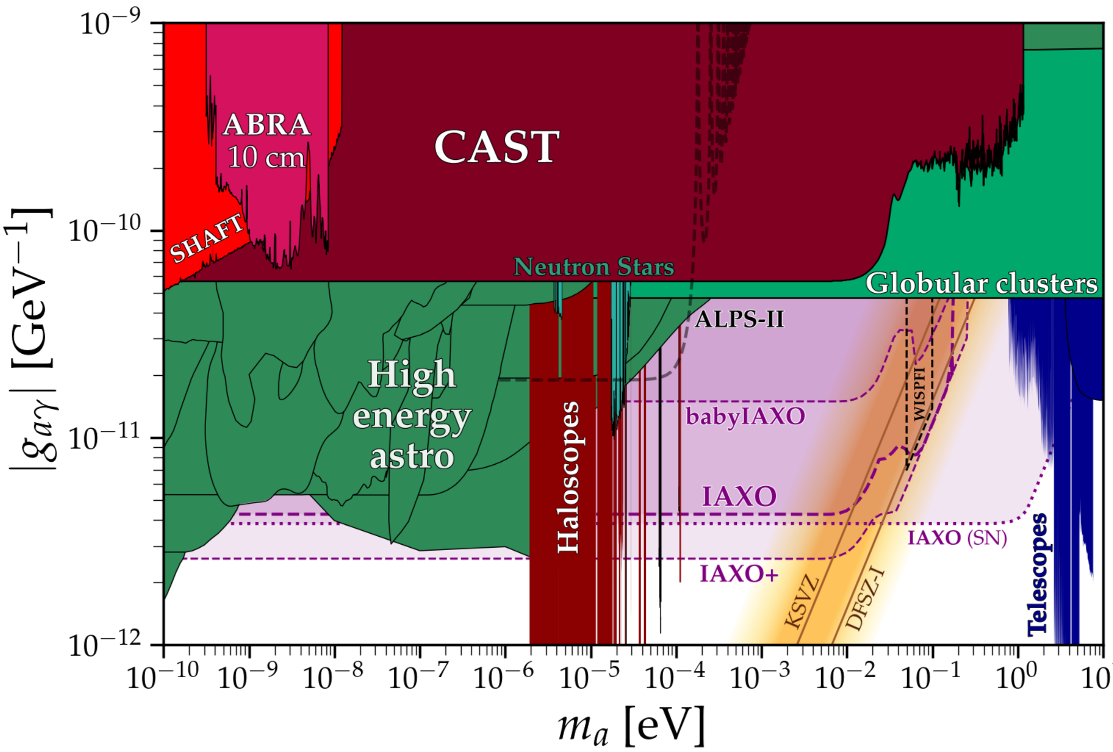

Figure 10: **Projected axion parameter space for IAXO**
The projected sensitivity of IAXO and BabyIAXO to the axion-to-photon coupling $g_{a\gamma}$ is depicted in comparison to other experimental limits. Both experiments aim to surpass current experimental limits and probe new regimes in the axion parameter space. Adapted from [33].

2.1. Goals

As a helioscope experiment, IAXO aims to measure solar Axions by utilising the inverse Primakoff-effect, coupling them to X-ray photons in a strong magnetic field, as described in chapter 1.2.3.

Its predecessor, CAST, reached unprecedented goals during operation, being the first helioscope to surpass the astrophysical limit on the axion-to-photon coupling $g_{a\gamma} \lesssim 10^{-10}$ GeV^{-1} [43]. IAXO is aiming to surpass those limits by incorporating only custom-built components. CAST, on the other hand, was built mainly from recycled components, like an old X-ray satellite, used for the optics system [45]. A visual representation of the aspired sensitivity for IAXO is shown in figure 10. IAXO will surpass astrophysical limits by more than one order of magnitude in the regime of a meV axion-mass. The custom-developed components will enable this improved level of sensitivity. The proposed sensitivity of BabyIAXO, the prototype experiment for IAXO, is shown in figure 10.

Figure 11: **Conceptual design for BabyIAXO**
BabyIAXO will consist of a smaller magnet than IAXO, with two bores with a length of 10 m. The magnet system is visible as a yellow cylinder. Two tubes coming out of the bottom part of the magnet system depict the X-ray-focusing telescope. Two different detector systems, encased in special shielding, are shown at the end of the structure. The model is placed at the future BabyIAXO site in the HERA South Hall. Next to the model, the first parts of the BabyIAXO drive system can be seen as red tubes on the bottom right. Image from [46].

2.2. BabyIAXO

BabyIAXO is a transitional step between CAST and IAXO concerning its goals and technological complexity. While CAST was mostly constructed from recycled parts, like the LHC dipole magnets, and IAXO will use fully custom-developed parts for maximum sensitivity, BabyIAXO utilises some recycled components from old experiments, like the structure and drive system, but also some custom components, like a custom magnet system.

BabyIAXO will be constructed in the HERA South Hall at DESY in Hamburg. Figure 11 shows a 3D concept of the BabyIAXO helioscope in the proposed location at the HERA South Hall. BabyIAXO will function as a fully operational axion experiment, aiming to push sensitivity levels down to $g_{a\gamma} \sim 1.5 \times 10^{-11}\mathrm{GeV}^{-1}$ and probe a new parameter space. This is especially relevant for the high mass region, where BabyIAXO will probe part of the QCD axion band. This also includes finding or excluding KSVZ axions in a mass range between 70 and 250 meV. [47] The results obtained from BabyIAXO will be valuable for the construction and further development of IAXO.

This way, BabyIAXO can save time and money by not re-developing suitable components that already exist and fit all necessary requirements, but still push sensitivity limits, by implementing cutting-edge technology where it is most crucial. The main parts of the BabyIAXO experiment are the following [47]:

- **Structure and drive system:**
  For the structure and driving system, parts of the Medium-Sized Telescope (MST) of the Cherenkov Telescope Array (CTA) are repurposed since they have similar requirements in tracking sensitivity and weight capacity. The load on the drive system of BabyIAXO will be 71.6 t. The structure will allow BabyIAXO to achieve 12 hours of solar tracking time, coinciding also with the operational target set for IAXO. The most important parts of the structure and drive system are the foundation, the tower, the rotating head, the counterweights, and a large support frame. Most of the structure and drive system parts are already in the HERA South Hall.

- **Custom superconducting magnet system:**
  One of the main improvements of BabyIAXO, in contrast to CAST, is the custom-developed superconducting magnet system. A good metric for evaluating the magnet system is the magnet figure of merit $f_M = B^2L^2A$, where B is the magnetic field, L is the length, and A is the cross-section area. The CAST magnets have already achieved a magnetic field strength of 9 T and a length of 10 meters, so enhancing these parameters presents significant challenges. However, the magnet's design results in a relatively small cross-section area of just 0.003m^2. With a different magnet configuration, a substantially larger cross-section is possible [48]. Therefore, the magnet system for BabyIAXO comprises two 10 m long and 82 mm thick racetrack coils with two bore tubes between them. With a peak field of 3.2 T, the magnetic field strength is lower than the 9 T field of CAST [49]. The combined cross-section area, however, is increased from 0.003m^2 to 0.77m^2. This improves the magnet figure of merit by more than an order of magnitude compared to CAST.

- **Cryogenics for superconducting magnet:**
  The BabyIAXO cryostat is essential for the operation of the custom superconducting magnets. It is primarily constructed from aluminium alloy in a cylindrical shape due to relatively low mass and manufacturing costs. The cold mass is supported by a system of titanium and Permaglas rods, which minimises heat loads and ensures stability, even during inclinations of up to $\pm 25°$.

Cooling is achieved using a "dry" system that employs cryocoolers and helium gas circulators, enabling a cooldown from room temperature to 4.2 K in approximately 17 days.

- **X-ray focusing optics:**
  The X-rays generated in the magnetic field are focused by the optics to the detector. To maximise the experimental outcome, each of the two bores will be equipped with different X-ray optics. The first one will implement an existing flight-spare module from the X-ray Multi-mirror Mission (XMM) Newton. These optics were designed for a comparable telescope diameter. They are a promising and, in XMM, already successful set-up [50]. The second bore will implement a custom-designed focusing optic set-up, similar to the final IAXO optics. [51]

- **Detector:**
  BabyIAXO will implement different detector technologies ranging from well-established axion helioscope detectors, like Micromegas, to newly developed high-sensitivity detectors, like Silicon Drift Detectors (SDD). The properties of the different detectors and the BabyIAXO detector requirements are elaborated in chapter 2.3. By integrating different types of detectors, BabyIAXO aims to improve the overall sensitivity across a broad range of axion masses. The active and passive shielding configuration is also an essential part of the detector setup.

All of the above mentioned components are already in development by designated subgroups of the IAXO Collaboration.

2.3. Detector Challenges

The main challenge of developing a detector for BabyIAXO is reaching the high sensitivity necessary for measuring an axion signal. To evaluate the quality of a detector, a simplified detector figure of merit (f_D) can be defined as:

$$f_D = \frac{\epsilon}{\sqrt{b}} \tag{12}$$

Here, the detection efficiency is denoted as ϵ, and b is the normalized background of the detector. This equation shows that for achieving a high f_D, the key aspects of a detector are maintaining low background levels while achieving a high detection efficiency. Considering that BabyIAXO expects just a couple of axion counts per year for an axion-photon coupling of 10^{-11}GeV^{-1}, it is essential to maintain ultra-low background levels to avoid drowning the signal. Passive (lead, copper, or borated plastic) and active (scintillating plates) shielding techniques are used to reach the low background Goal of $10^{-7}\text{cts}/(\text{cm}^2\text{s keV})$ for BabyIAXO. The energy range of interest for BabyIAXO matches the Primakoff spectrum in figure 6, which is the axion flux BabyIAXO wants to detect. This means the detector must have an especially high detection efficiency for X-rays in the low keV range. The Primakoff spectrum peaks at approximately 3 keV, making high sensitivity in this range particularly important. A high sensitivity around 1 keV is also desirable, as a large part of the axion flux from axion-to-electron coupling is in this range. In contrast to the Primakoff spectrum, the ABC spectrum would also benefit from a good energy resolution to resolve the numerous peaks in the spectrum. Therefore, multiple detector systems are currently being developed.

The four main detector types currently under development for BabyIAXO are:

- **Micromesh Gaseous Structure** (Micromegas) detectors are small time projection chambers (TPCs) equipped with a Micromegas readout at the anode. This detector works by converting X-ray photons into detectable free charges within a gas-filled conversion volume. Micromegas was already tested at CAST, where it reached a background level of $10^{-6}\text{cts}/(\text{cm}^2\text{s keV})$[52].

- **GridPix** is an evolution of the Micromegas detector, where a photolithographically produced mesh is integrated with a pixelated readout chip, where the timePix3 chip is used[53]. This enables detecting a single electron being liberated by an interacting X-ray photon with small feature sizes and accurate alignment. The maximum detection efficiency for the GridPix detector is $\epsilon = 0.8$. [54]

- **Metallic Magnetic Calorimeters** (MMCs) detect a change in magnetic flux created by a temperature increase resulting from the deposited energy of a particle. This detector is operated at temperatures below 30 mK and has an especially fast response time in the order of 100 ns and excellent energy resolution of 1.6 eV for 5.9 keV photons [55].

- **Silicon Drift Detectors** (SDDs) are a type of semiconductor detector and the central part of this thesis. SDDs are expected to have an especially high detection efficiency of just below 100% [56], a good energy resolution of 140 eV [57] and low background potential in the order of 10^{-7} cts/ (cm^2 s keV) [58]. They are explained in more detail in the following section.

BabyIAXO will incorporate multiple detector systems. This way, they can be optimised for the future IAXO experiment.

2.4. Tristan SDD for IAXO

A promising possibility for a BabyIAXO and later IAXO detector is based on a silicon drift detector (SDD) from the TRISTAN [59] production. As part of KATRIN [60], the TRISTAN project is developing a detector to measure the entire electron spectrum of the tritium beta decay. While KATRIN currently measures near the endpoint energy to determine the absolute neutrino mass, the new TRISTAN SDD will allow KATRIN to search for sterile neutrinos by analysing the whole tritium spectrum. With minimal additional development, the TRISTAN SDD for IAXO (TAXO SDD) has the potential to meet all requirements needed for an IAXO and BabyIAXO detector.

2.4.1. Silicon Drift Detectors

A silicon drift detector is a type of semiconductor detector. The electrical properties of semiconductors lie between those of insulators and conductors. One of the main advantages of silicon as a semiconductor material is its thermal stability, allowing silicon drift detectors to be operated at a wide range of temperatures without a loss in performance. As a semiconductor, silicon can also easily be doped to modify its properties.

The band gap of only 3.63 eV means that an electron-hole pair is created for every 3.63 eV deposited, resulting in a very good energy resolution due to a large number of charges. Intentionally introducing impurities to the silicon lattice can create additional states inside the band gap, altering its conducting properties. This process is called doping. [61]

There are typically two types of doping used in an SDD. Type-n doping introduces an additional energy level near the conductance band, which releases a free electron to the conductance band. In the case of silicon, being a group IV material in the periodic table with four valence electrons, a group V material like phosphorous will introduce an additional valence electron to the semiconductor material, creating an n-type semiconductor. Similarly, p-doping introduces an energy level near the valence band, creating a hole in the valence band by accepting an electron. This hole acts as a positive charge carrier. This is done by incorporating group III elements, such as boron, into the silicon. [62]

When a particle penetrates into the silicon volume, it generates an electron-hole pair at the interaction point. However, these free charges are indistinguishable from thermally generated charges in the silicon at regular temperatures. To ensure that an interacting particle produces a significant signal, its interaction region must first be depleted of free charges. This depletion zone can be created by using a reverse-biased p-n junction. Bringing p-type and n-type silicon into contact and applying

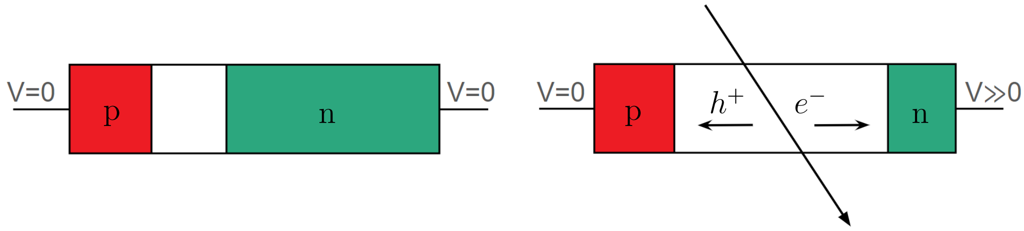

Figure 12: **Concept of a reverse biased p-n junction**
The enlargement of the white depletion zone in a p-n junction is shown. On the left, a p-n junction with no applied current is depicted. The p-doped material is depicted as a red region, and the n-doped material as a green region. In that state, the white, depleted region is relatively small. This white, depleted zone is enlarged on the right by applying a reverse bias. The applied voltage causes the negative charge carriers to move toward the anode, where they recombine, increasing the depleted volume. An incident ionizing particle can create an electron-hole pair, with the hole drifting to the p-doped and the electron to the n-doped material due to the electric field.

a negative voltage to the p-type and a positive voltage to the n-type silicon, the electrons and holes near the junction recombine, forming a charge-free depletion zone. If an electron-hole pair is now generated within this depletion zone, the electron will drift towards the anode and the hole towards the cathode, resulting in a small but detectable current [61]. A visualisation of a reverse-biased p-n junction is depicted in figure 12.

The working principle of an SDD is based on sideward depletion [56]. The SDD has a p-dotation on both sides of the chip. For a good energy resolution, a small n-doped anode is located in the centre of one side of the SDD. To drift the electric charges to the anode, the p-dotation is separated into concentric circles on which an electric field is applied [63], as seen in figure 13.

An advantage of the TRISTAN SDD is the additional integrated n-channel Junction Field Effect Transistor (nJFET) inside the anode of the detector chip for first-stage signal amplification [65]. The charge collected at the anode is proportional to the energy of the incident particle.

Most other detector types necessarily include some thick entrance window. Gaseous detectors like a Micromeags detector confine the detector gas with an aluminium foil with a thickness of at least $\mathcal{O}(\mu\text{m})$ [66]. In contrast, silicon as a detection material enables a thin silicon dioxide (SiO_2) layer with a thickness of just $d = 10$ nm and an additional thin transitional layer, in the order of 100 nm [67], to function as an entrance window [68]. This thin entrance window, compared to other technologies significantly increases the detection efficiency, especially for low keV X-rays.

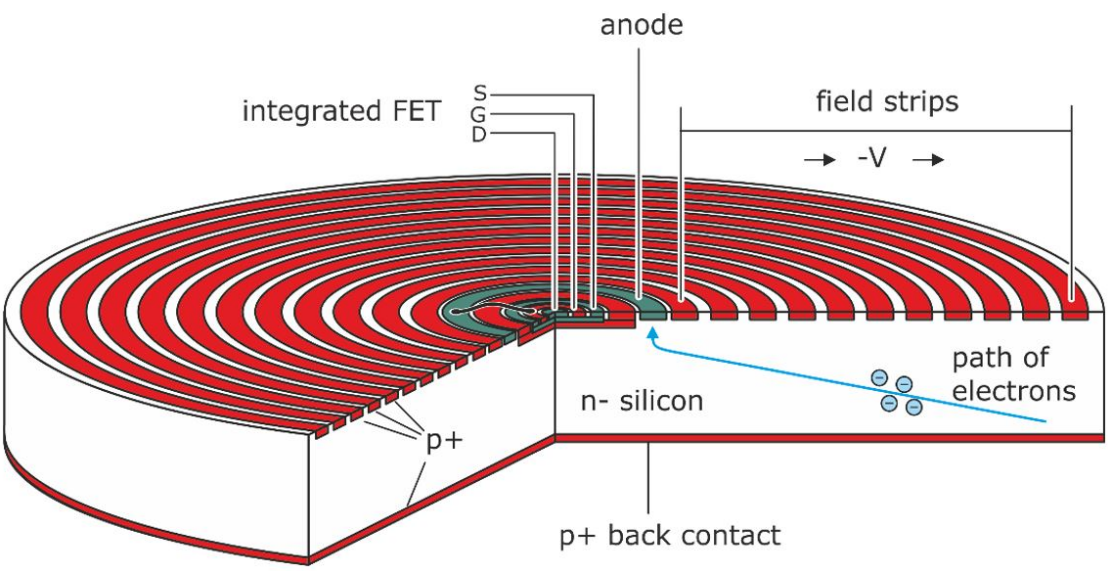

Figure 13: **Schematic diagram of an SDD**
The path of the electrons, created by incident energy, is visualised in blue. The back contact side of the SDD, as well as the drift rings, are made out of p$^+$ doped material (red). The bulk material is n$^-$ doped and shown as a white area. The anode in the centre of the SDD is shown in green. Scheme adapted from [64].

2.4.2. 7-Pixel TAXO SDD

The seven-pixel TRISTAN SDD is the basis for developing a detector for BabyIAXO. The project name for developing this detector is TRISTAN for IAXO (TAXO). The SDD comprises seven hexagonal pixels with a respective diameter of 3 mm. The SDD is 450 μm thick with deadlayer in the order of 50 nm [69]. In the TRISTAN prototype, the detector chip, ETORE ASIC [70], and the necessary electronic connections are mounted on a rectangular printed circuit board (PCB), as seen in figure 14. This detector board was also used for the detection efficiency measurement, explained in

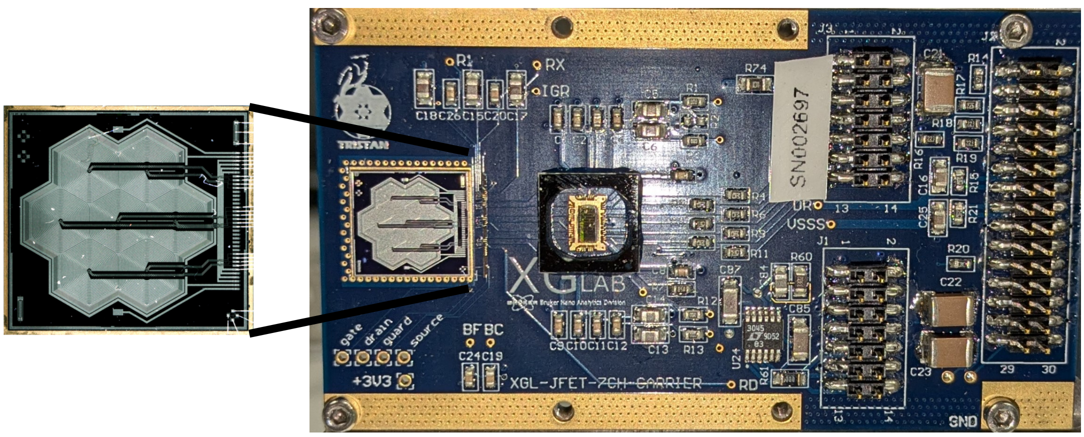

Figure 14: **TRISTAN seven-pixel SDD**
The seven-pixel silicon drift detector with a 3 mm pixel diameter is mounted on a printed circuit board (PCB). A closer view of the seven pixels with the corresponding read-out connections is shown on the left.

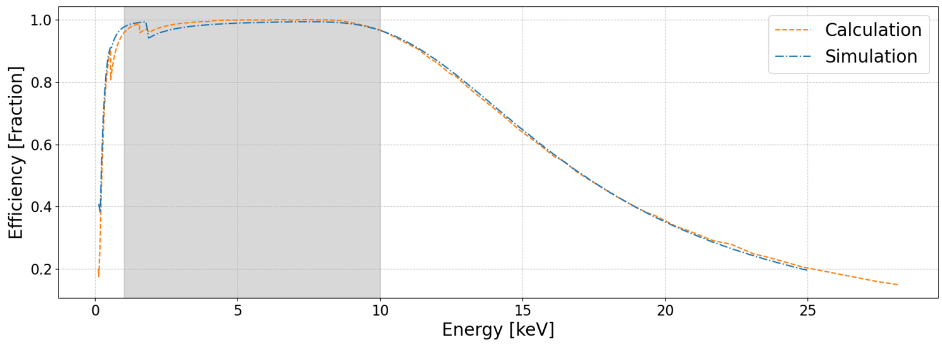

Figure 15: **Theoretical SDD detection efficiency**
A calculated efficiency is shown as an orange dotted line (data taken from [56]). The TAXO internal GEANT4 simulated efficiency is shown as a blue dotted line [71]. The shaded grey area indicates the energy range with the highest flux of solar axions.

chapter 3.

Even though, this detector was initially designed for application in the KATRIN experiment, it has excellent properties for using it in a rare event search, such as a helioscope looking for solar axions.

One of the most essential properties of a detector that is suitable for integration into BabyIAXO is its high detection efficiency in the energy range of interest. Most of the solar axion flux is in the energy range of 1 to 10 keV, as described in Chapter 1.2.3. For the final implementation in the BabyIAXO experiment, the shape and material of the PCB are continuously improved for an increased background performance.

A theoretically determined detection efficiency of a silicon drift detector with a thickness of 450 μm is shown in figure 15. Both calculations and TAXO internal simulations point to an excellent SDD detection efficiency of 99% for X-rays of the Primakoff spectrum and 92% for the ABC spectrum. The main task of this thesis is to check if this expected efficiency can be achieved with the TAXO SDD.

Figure 16: **SOLEIL synchrotron facility**
This photograph shows the main building, housing the synchrotron and its associated beamlines. They are the facility's core infrastructure.

3. Efficiency Measurement

To determine the absolute detection efficiency of the SDD, I had the opportunity to take measurements at the Metrology beamline of the SOLEIL Synchrotron facility.

3.1. SOLEIL

SOLEIL is an ultra-high-tech facility for academic research and industrial uses located at the Paris-Saclay University and Technology Park. The main building, housing the Synchrotron and all beamlines can be seen in figure 16. It provides high-intensity synchrotron radiation for applications ranging from condensed matter physics to astrophysics.

3.1.1. The Synchrotron

The SOLEIL synchrotron creates synchrotron radiation, from infrared to hard X-rays, by accelerating electrons. They are first accelerated in a LINear ACcelerator (LINAC) to an energy of 100 MeV. Then, they are injected into a Booster ring, further accelerating them to an energy of 2.75 GeV[73]. Finally, they are injected into a storage ring with a circumference of 354.097 m [74], where they maintain an energy of 2.75 GeV. From there, they produce radiation through Wigglers, Undulators, or Dipole magnets for the many beamlines around the Storage Ring [73]. The whole structure, including the accelerators and all beamlines, is depicted in figure 17.

Around the storage ring, there are 29 beamlines. Each one is optimised for different applications with different photon energy ranges. Figure 18 illustrates the energy range covered by each beamline and gives an overview of the beamline distribution

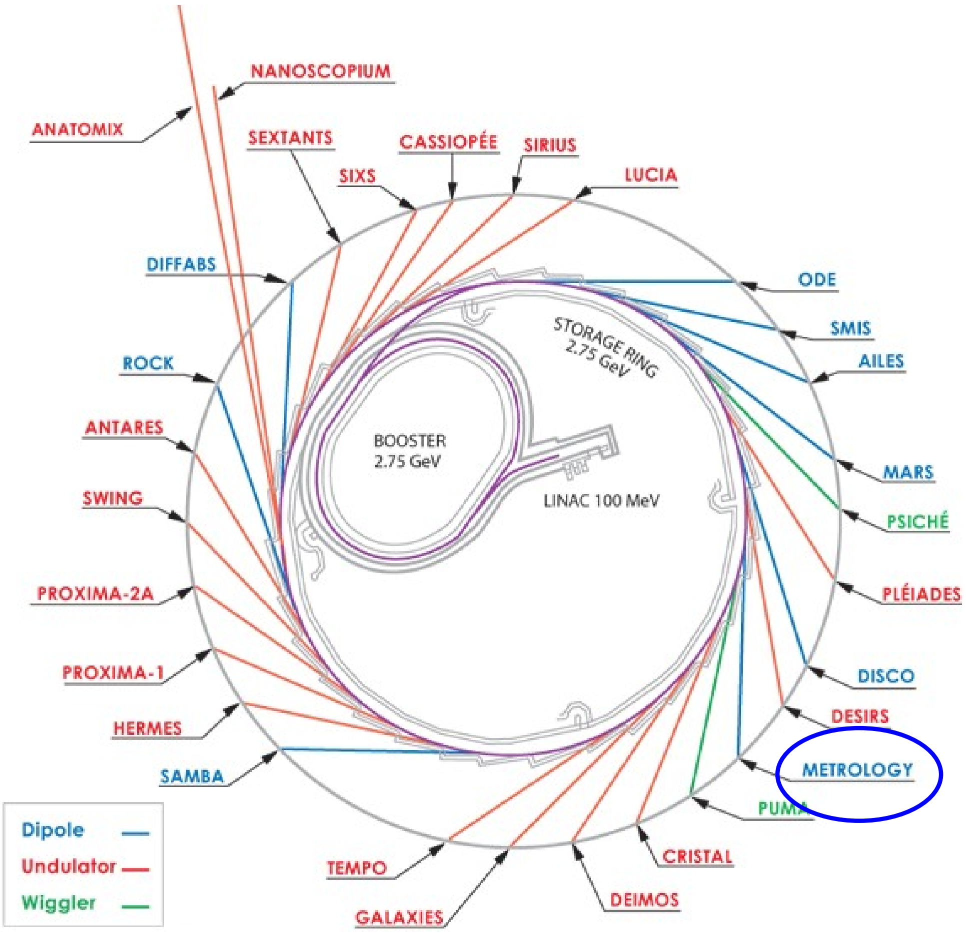

Figure 17: **SOLEIL synchrotron beamlines**
This diagram shows the position and name of the different beamlines around the storage ring at the SOLEIL Synchrotron. The device for creating the beams at the individual beamlines is indicated by colour, where blue represents dipole magnets, red represents Undulators, and green represents Wigglers. The experiments for this thesis were conducted at the Metrology beamline, circled blue in the bottom right of the diagram. Taken from [72].

across the X-ray spectrum. The beamline with the largest energy range, spanning from very soft X-rays to hard X-rays, and the one at which I toke measurements is the Metrology beamline.

3.1.2. Metrology Beamline

One of the most versatile beamlines at SOLEIL is the Metrology beamline, built as a metrology test facility for the R&D of optical components and detectors. The X-rays for the Metrology beamline are produced by the bending magnet D05-1°. The beam is then distributed onto two specialised beamlines in two different energy ranges, which can be operated in parallel.

The first beamline branch is for soft X-rays in the energy range from 300 eV to 2 keV and has an acceptance angle of 2 mrad $\times$ 0.48 mrad, horizontally and vertically, respectively. Three concave mirrors redirect and focus the beam along the beamline.

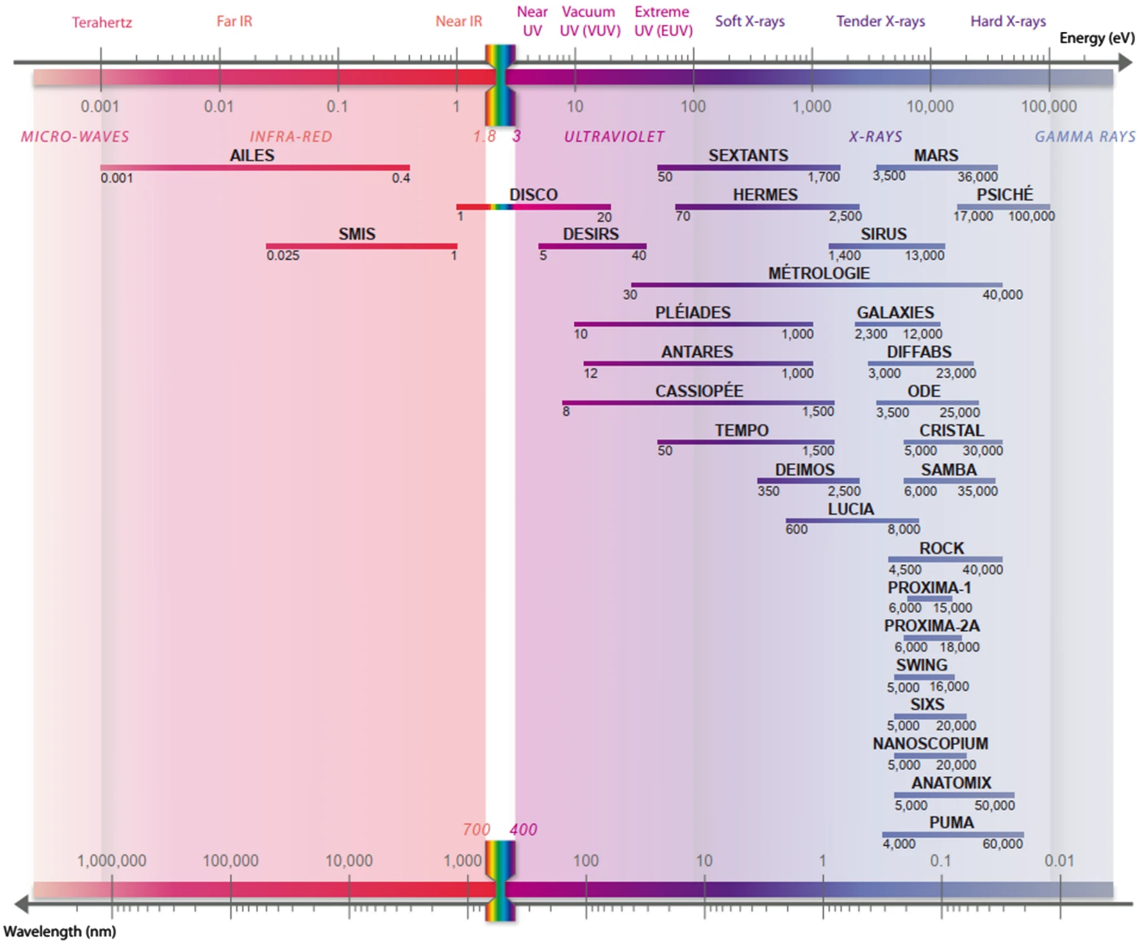

Figure 18: **Beamline distribution across different energy ranges**
The beamlines around the SOLEIL synchrotron are distributed across different energy ranges, mostly in the X-ray spectrum. Taken from [73].

The photon energy is selected with a Varied Line Spacing Plane Grating Monochromator (VLS-PGM) between the second and third mirror [75]. This monochromator uses the converging beam from the second mirror and three interchangeable gratings with different groove densities for various energy ranges [76].

The second beamline branch is for hard X-rays in the energy range from 3 keV to 35 keV and has an acceptance angle of 1.7 mrad × 0.153 mrad, horizontally and vertically, respectively. The data used for the analysis, described in Chapter 4, were taken at this branch. Here, a double-crystal monochromator (DCM) is used for the energy selection and tuning of the desired beam intensity. In this beamline, the DCM is located 21 m from the bending magnet. It uses two Si(111) crystals to select the beam's energy. The first crystal changes the continuous synchrotron spectrum into a narrow wavelength spread, while the second crystal makes the transmitted beam parallel to the incident beam. This second crystal is commonly detuned, making it slightly unparallel to the first crystal to decrease the bandwidth and suppress harmonic contaminations as much as possible [77].

The harmonics occur at 3 and 4 times the main energy. The reason for the occurrence of harmonics is that a DCM relies on Bragg diffraction, see equation 13, where the multiples of a desired energy also satisfy the diffraction condition.

$$n\lambda = 2d \sin\theta \tag{13}$$

The first harmonic at twice the energy is highly suppressed because its structure factor is zero. This means that the scattering vectors from atoms in the unit cell of the crystal interfere destructively, cancelling each other out. [78] The harmonic contribution is less relevant for higher energies since it decreases more rapidly for high than low energies [77]. In our measurements at the metrology beamline, we also observed harmonics, as described in Chapter 4. Although they introduce some errors, the intensity of the harmonics is low enough that they do not significantly affect the results.

After the wavelength selection, an elliptical mirror M1, an exit slit, and a flat bendable mirror M2 focus the beam at the sample location. All primary optics can also be translated out of the beam for measurements with the synchrotron radiation white beam [77].

The beamline also includes a high vacuum chamber, shown in figure 19, with a moveable $d = 55.5$ μm thick AXUV100TF400 photodiode mounted on the far side of the beam. In our efficiency measurement, this photodiode is used for the determination of the absolute rate. A two-axis motorised goniometer is located at the centre of the vacuum chamber. The beam target, in this case a holder with the SDD, can be mounted onto the goniometer, allowing a precise positioning within or without the beam's path.

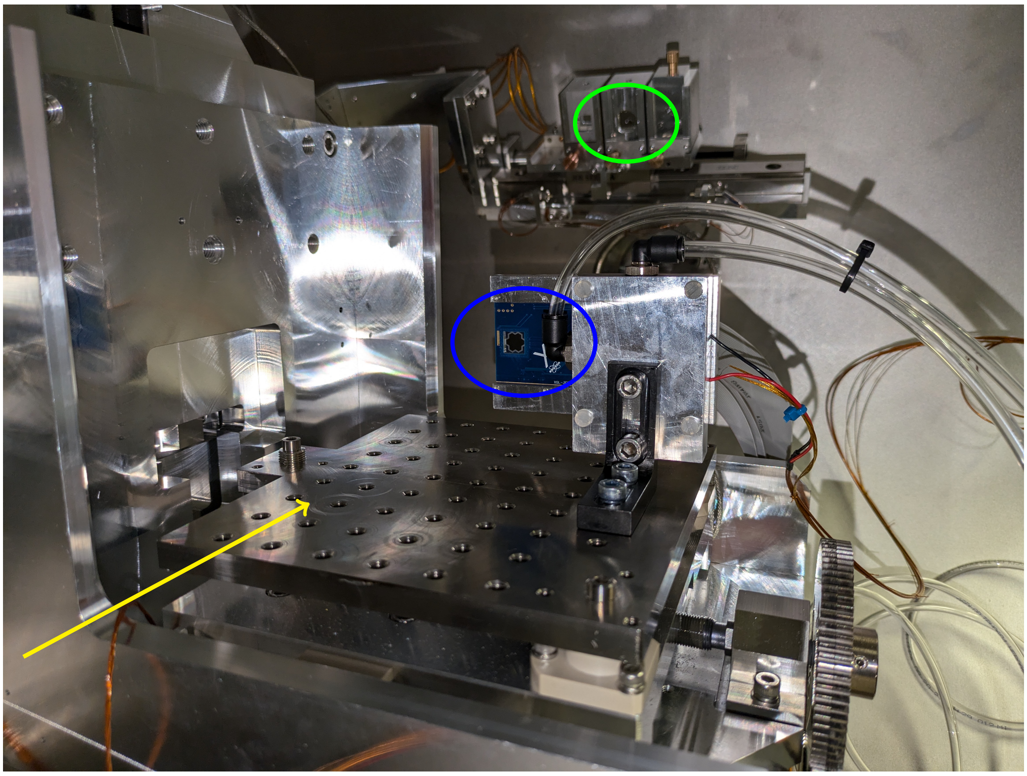

Figure 19: **Vacuum chamber for the hard X-ray branch of the Metrology beamline**
This photograph was taken from the inside of the vacuum chamber of the hard X-ray branch of the Metrology beamline. The two-axis goniometer can be seen at the bottom, the SDD, circled blue, is mounted onto it in the centre with a holder. The photodiode, circled green, is located at the centre of the vacuum chamber, visible in the centre top part of the photo. During operation, the photodiode is lowered into the beam's line of sight. The yellow arrow marks the direction of the beam.

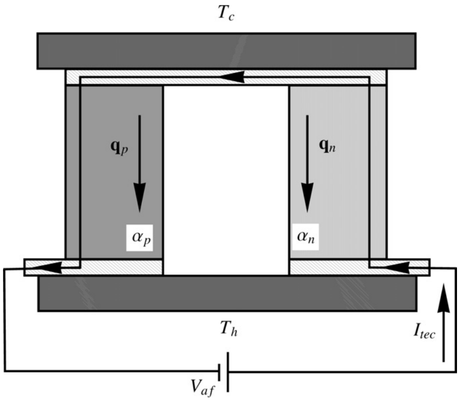

(a) q_n and q_p are p- and n-type materials with α_p and α_n as their corresponding Peltier coefficient, and T_c and T_h are the cold and hot side of the thermocouple. An external voltage V_{af} is applied [79].

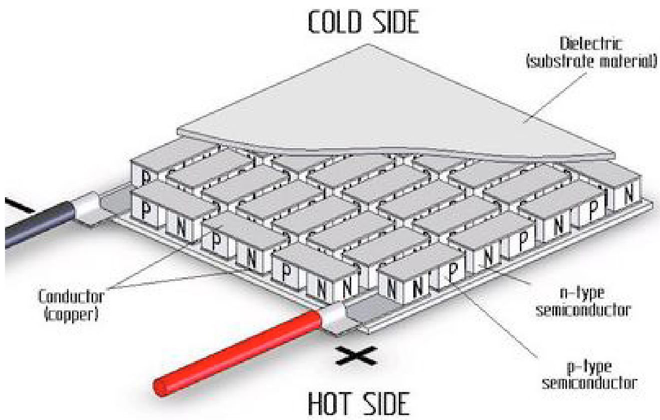

(b) Structure and composition of a Peltier cooling element. Adapted from [81]

Figure 20: **Peltier element Concept**
This figure depicts the working principle of a Peltier cooling element. In (a), a single detailed thermocouple cell is depicted. In (b), the serial connection of many thermocouple cells, building a Peltier element, is portrayed.

3.2. SDD Holder and Cooling System

I designed a custom holder to securely attach the SDD PCB to the goniometer and position it vertically in the beamline. Good thermal contact between the PCB and the holder is important for an efficient heat drain since the operation of the SDD also produces heat. A cooling system via a Peltier element was included in the holder, to improve the energy resolution of the SDD.

A Peltier element, also called a Peltier thermoelectric cell, is a cheap and reliable tool for small-scale refrigeration. It comprises many thermocouples (TCs), as shown in figure 20a, thermally connected in parallel and electrically in series [79]. It relies predominantly on the Peltier effect, which describes the heat transport from one side of a TC to the other through an electrical current. This results in the cooling and heating of each junction, respectively.

The quality of the heat transfer depends on the difference in the Peltier coefficients of the materials between the junctions. The Peltier coefficient, in turn, depends on the electron density of a material, among other parameters. This is why p- and n-type semiconductors are commonly used in Peltier elements. [80]

The holder consists of a metal block comprising the heat drain system and a c-shaped part where the SDD is mounted. The Peltier element is positioned between the components using fitted indents. The element is kept in place by the pressure created when both sides are fastened together with screws. The heat transfer through the

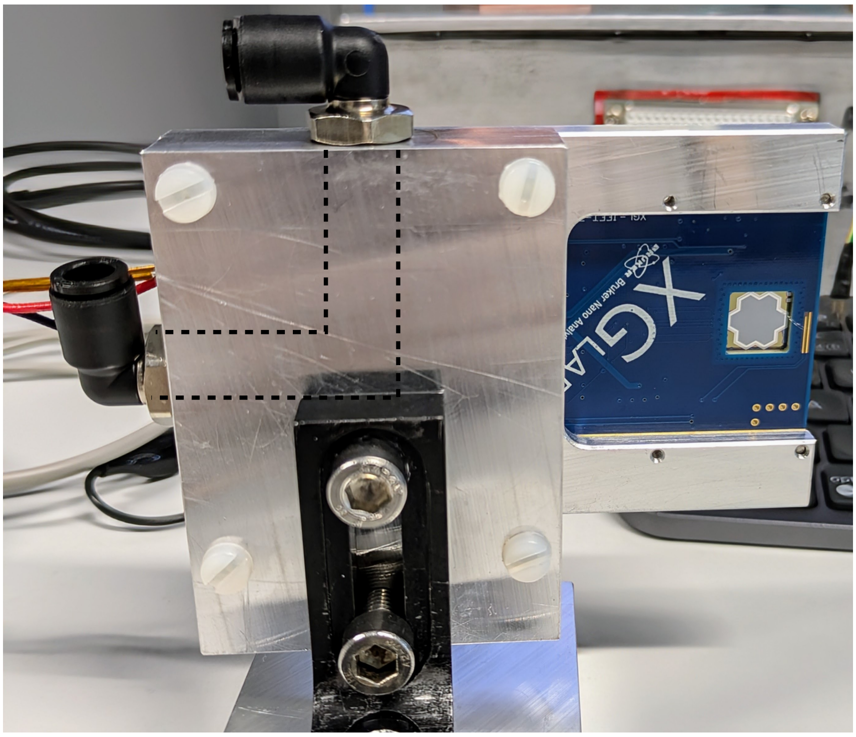

Figure 21: **Holder for SDD with included cooling and heat drain system** The aluminium holder with mounted SDD on the blue PCB is depicted. The shape of the seven hexagonal pixels can be seen through the hole of the PCB. The black adapters for a water heat drain system are visible on the top and on the left-hand side of the central aluminium block. The dashed lines in the photo indicate where the water can circulate through drilled holes. The holding structure is attached to the surface by a simple metal angle.

screws between the hot and cold section of the holder is minimised by using special PEEK screws. PEEK is a high-temperature-resistant plastic [82]. The heat transfer is maximized between each section of the holder and the respective side of the Peltier element via a thermal paste.

A water cooling system was included in the metal block to reach even lower temperatures with the Peltier cooling. Aluminium was used as material for the holder, due to the effectiveness of the water cooling. In the first tests under non-vacuum conditions, the limit of the Peltier cooling system was 0 °C due to the thermal conduction of the air. In a vacuum chamber under a pressure of $\sim 10^{-7}$ mbar, the system could reach temperatures of -15 °C. This temperature was maintained in the measurements, even during the SDD's operation.

The final version of the holder with integrated Peltier cooling, water heat drain system, and the mounted SDD-PCB can be seen in figure 21. This setup allows the SDD to maintain a good energy resolution by keeping its operating temperature below 0°C.

3.3. Experimental Setup

Before the measurements at the Metrology beamline could be conducted, first the experimental setup was developed. For this, all necessary electronic components were selected and configured.

3.3.1. Data Acquisition

The data acquisition describes how the data is taken and the components necessary for processing it. The composition and connection of all components should enable a signal transfer from the moment a photon hits a pixel of the SDD, then amplifying the signal, identifying it as an event and converting it to digital data, which can then be stored on a computer. The data acquisition process for the measurement at SOLEIL is visualised in figure 22. These were the main components of the setup:

- SDD
- Bias board
- NIM Pulse generator
- Dual channel waveform generator
- CAEN V1782 Octal Digital Multi Channel Analyzer
- PC

The signal from the SDD is first transferred to the bias board. It is connected to the detector by flat cables. For these measurements, I used a bias system developed by XGLab. The bias system is required to provide and control all detector biases. Additionally, it induces a pulsed reset signal for a synchronised discharge of the SDD capacitors. An external pulse generator was used to define the reset period in this

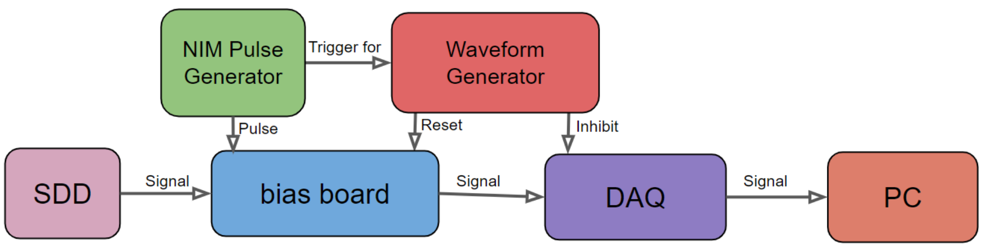

Figure 22: **Signal processing chain and experimental setup**
In this diagram, the composition of the experimental setup and its connections are depicted. The amplified signal from the SDD gets transferred to the bias system for further amplification. The data acquisition (DAQ) system converts it to a digital signal. The NIM pulse generator and the dual waveform generator are responsible for the timed read-out and inhibit signals. Finally, the data is transferred to a PC, where it can be stored for further analysis.

Figure 23: **CAEN data acquisition card**
The CAEN V1782 Octal Digital Multi-Channel Analyzer, operating as a data acquisition (DAQ) system, converts analogue signals into digital data. The DAQ system is connected to the bias board to transfer the SDD's signal. Another input is the inhibit pulse from the waveform generator. The output is an optical fibre cable connected to a computer [83].

measurement. The bias board can also receive another external pulse and induce it as a signal on every pixel of the SDD. The bias board is powered by an external power supply, providing 25 V and 1.5 A.

The output signal from the bias board is received by the data acquisition (DAQ) card. For this measurement, a CAEN V1782 Octal Digital Multi Channel Analyzer, depicted in figure 23, was used as a DAQ card. A second input for the DAQ card is a pulsed inhibit. It is necessary to inhibit the signal during the discharge of the SDD capacitors, as output distortion can affect the signal processing and identification. In the DAQ card, the analogue signal is turned into computer-processable digital data. It is connected to a desktop PC via optical fibre cables for data transfer and configuration.

A dual channel waveform generator is used for creating the reset and the inhibt signal. Both are created by the same device to synchronise the two pulses. The first channel defines the inhibit and has a pulse length of just 5 μs. The second channel defines the timing and duration of the inhibit and has a pulse length of 50 μs. The pulse in both channels gets externally triggered by another pulse generator.

A NIM model pb-5 pulse generator is used as the external trigger for the reset and inhibit. The primary function of this pulser is to induce an additional signal in the SDD, which acts as a crucial part of the analysis, described in Chapter 4. This pulse is set to a rate of 1 kHz and an amplitude of 0.19 V, correlating to an energy of approximately 23 keV in the SDD's energy spectrum. This pulse is timed to occur

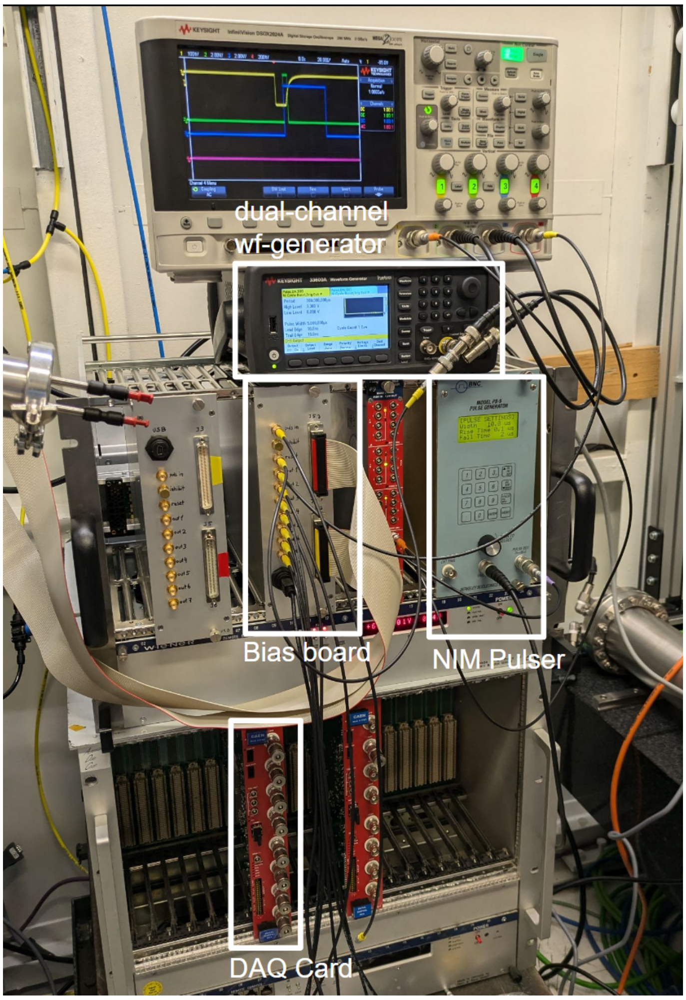

Figure 24: **Components for data acquisition**
For the data acquisition, a bias board, a CAEN V1782 DAQ card, a dual-waveform (wf) generator, and a NIM model pb-5 pulse generator (pulser) were used.

slightly before the induced SDD reset via the provided external trigger signal to the dual-waveform generator. In figure 24, the assembly of these components and their connections are shown.

3.3.2. Data Processing

Most of the processing of an event from the detector happens in the DAQ card. Here, the signal is discriminated from the background using digital signal filters. In this DAQ card, the event trigger is set via an RC-CR2 filter and the amplitude is recreated through a trapezoidal filter.

The DAQ card can be operated in waveform mode and in list mode. The list mode saves only the analysed data in a list of specific information about each event. The advantage of this mode is its rapid operation, as it only requires writing the essential information for each event to the storage medium. This mode was used for the data acquisition during the measurement at the SOLEIL synchrotron.

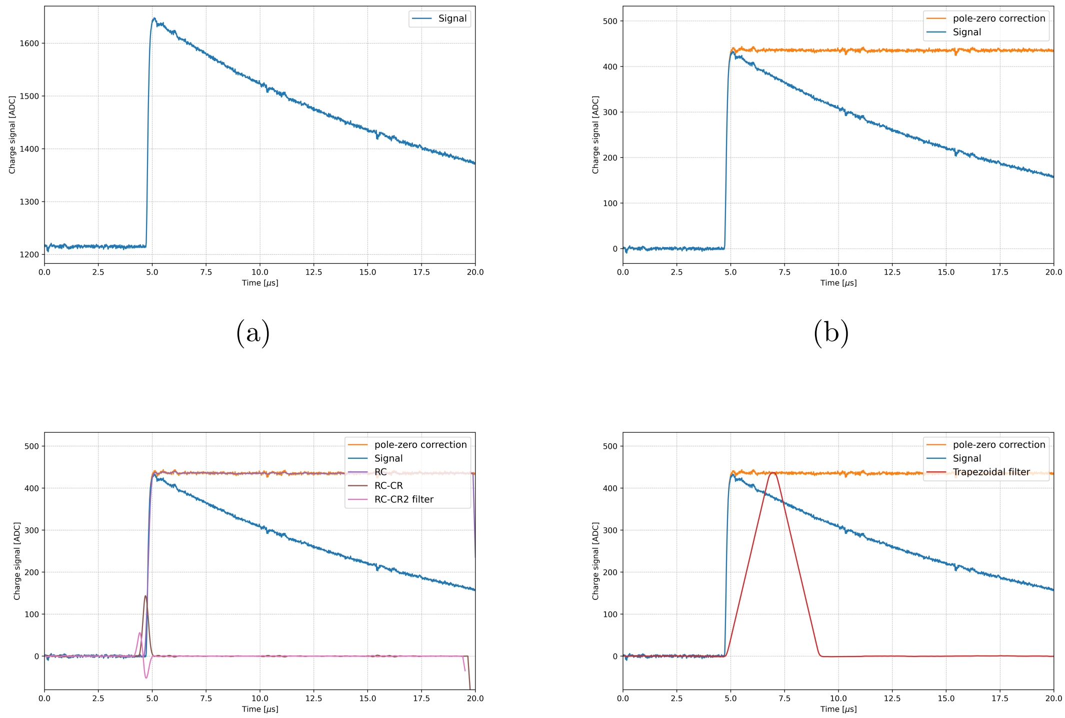

(a) (b)

(c) (d)

Figure 25: **Sample waveform analysis**
The filtering process, applied in the data processing of a CAEN V1782 DAQ card is visualised in this diagram. The processing is illustrated on the waveform of an exemplary detector emulator event simulating an SDD X-ray event. The raw waveform is depicted in the top left panel. The top right panel visualises the baseline restoration process and pole-zero correction (orange) on the waveform. The bottom left panel shows the applied RC-CR2 trigger filter. In this panel, the consecutive application of a window averaging filter (purple) and then twice a derivation filter (brown and pink, respectively) on the signal is visualised. The bottom right panel shows the application of a trapezoidal filter (red) for the energy determination.

The waveform mode, on the other hand, saves the whole waveform for every detected event. This not only increases the dead time due to a lot of data being processed but also results in large file sizes, even for short acquisition times. The advantage of this mode, however, is a better understanding and visualisation of the measured events. This is very valuable for understanding the working principle of the event selection. This is especially relevant for measuring the absolute detection efficiency, where the number of detected events plays a major role.

The CAEN DT5810 Fast Digital Detector Emulator can simulate SDD events. An example of such a waveform is shown in figure 25a, to visualise the working principle of the RC-CR2 and trapezoidal filter.

A baseline restoration is the first signal processing step, keeping the signal's shape but shifting it such that the baseline is at 0. In the next step, a pole-zero correction is applied to the signal. This keeps the event's amplitude but removes the exponential decay visible in the raw waveform. Figure 25b shows the applied baseline restoration and pole-zero correction.

Next, the RC-CR2 filter applies a window averaging and then twice a derivation filter to the signal, resulting in a sinus-like shape as seen in figure 25c. The trigger for an event is armed when the filter signal crosses a threshold value. The trigger is activated when the filter signal has a negative slope as it crosses zero while armed.

The trapezoidal filter reconstructs the event's amplitude. It operates by applying a differential window averaging filter to the pole-zero corrected signal. This is depicted in figure 25d. The trapezoidal filter is relevant for the energy determination of an event, as the amplitude of the signal correlates to the energy of the incident particle.

In the detection efficiency measurement, the here elaborated event identification and characterisation procedure is done internally by the CAEN V1782 DAQ card. The optimised configuration of the values for the filters needs to be set manually. The most important values are the rise time for both filters, the trigger threshold, the pole-zero decay time, and the window size for the baseline determination. The corresponding configuration was determined by a series of test measurements with the detector emulator.

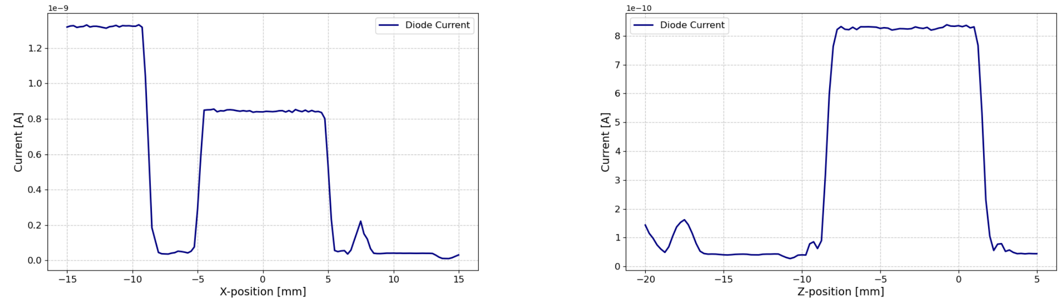

(a) (b)

Figure 26: **Positioning of the SDD**
The photodiode current was measured while moving the SDD vertically (a) and horizontally (b). The minimum intensity was measured when the beam was hitting the PCB. A step-like increase in intensity was seen when the beam was hitting only the thinner SDD chip.

3.4. Measurements

All data taking discussed in the following was done at the hard X-ray branch of the Metrology beamline at the SOLEIL facility due to noise issues at the soft X-ray branch. The data for the hard X-ray branch was collected over a period of two days.

The first challenge was the right positioning of the SDD so that the beam centrally hits the detector. This was done by measuring the beam intensity with the photodiode in the back of the vacuum chamber while moving the SDD for a sufficient distance horizontally and vertically, respectively.

In figure 26a the photodiode current during the horizontal positioning is shown. In the current, the composition of the detector is visible as a change in the current intensity. From left to right, the beam intensity changes from a very high intensity of the unobstructed beam to a very low intensity, corresponding to the beam hitting the thick PCB. A noticeable increase is seen when the beam spot moves from the thick PCB to the thin silicon detector. After that, on the right side of the plot, the intensity decreases when the beam is, again, hitting the PCB.

The same process is done for the vertical positioning, visible in figure 26b. Due to the limited scanning range, only the change in intensity between the beam hitting the PCB and the SDD is captured.

Both scans were used to calculate the X- and Z-position for the beam hitting the centre pixel of the SDD. Those values for the goniometer were determined to be $X = 0.1$ mm horizontally and $Z = -3.4$ mm vertically.

After the detector positioning, the next step was to tune the beam intensity. For the detection efficiency measurement, a rate of approximately ~ 10 kHz was desired, which is relatively low for the SOLEIL Synchrotron's typical operating conditions of

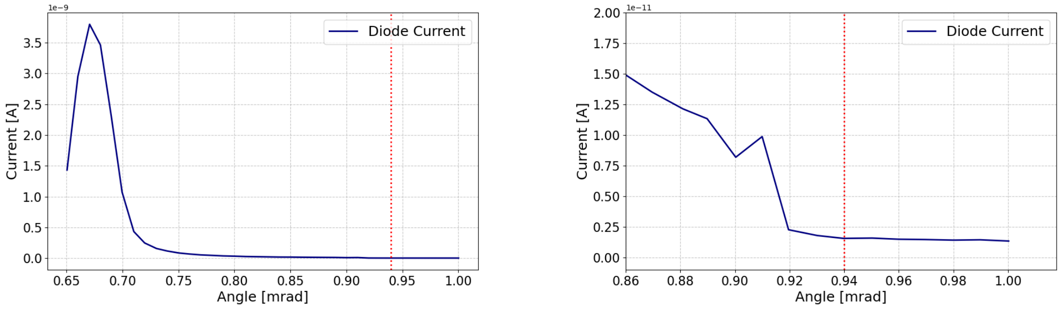

Figure 27: **Beam intensity scan**
The beam intensity was adjusted by moving the second crystal of the DCM. A full view of the intensity range at a beam energy of 12 keV can be seen in the left panel. In the right panel, a small section of the full range is shown to better display the region of interest. The selected angle of 0.94 mrad is marked by a dotted line.

up to GHz rates [84]. The rate tuning is done by adjusting the angle of the second crystal of the DCM. The change in beam intensity with a changing crystal angle can be seen in figure 27.

Such a scan of the beam intensity over the crystal angle is called a *Rocking Curve*. For the purpose of this measurement, only the tail of the Rocking Curve was used, which translates to using only the outer edges of the beam, resulting in a reduced photon rate. A diode current of approximately 2×10^{-12} A was targeted, resulting in a beam rate within the desired range. This angle had to be tuned every time the energy was changed since an energy change shifts both crystals of the DCM, resulting in a necessary adjustment of the second crystal for the desired beam intensity.

At this point, the beam was tuned to the right rate and hitting the SDD at the centre. Unfortunately, when attempting to collect the initial data, a noise issue was identified. Some light was emitted from the motorised positioning system of the two-axis goniometer. Even though the light is low in energy compared to the beam, the ultra-thin entrance window of this SDD allows it to pass through easily, leading to almost immediate saturation of the detector. This would make data-taking impossible.

The solution to this problem was switching the power supply to the motors completely off during the SDD measurements. The SDD had to be moved out of the beamline, for the comparison measurement with the photodiode. Therefore, the power supply for the positioning motors had to be switched on and off for every measured data point. This solution effectively resolved the noise issue, allowing measurements to be taken.

With these given requirements, a measurement procedure was developed. All data points were performed in the following sequence. Before data collection, an outline was created to determine an appropriate number of data points and the specific energies at which measurements would be most reasonable. At the beginning, The SDD is positioned outside of the beam.

1. The first step of all measurements was to change the beam's energy by changing the DCM's angles, as described in section 3.1.2.
2. Next, the Rocking Curve was used to define the pitch angle for the second DCM crystal. This adjusts the beam intensity to a reasonable level, ensuring a consistent rate across all runs.
3. The first data was taken with the photodiode. At this point, the SDD was still out of the beam's line of sight to have an unobstructed beam intensity measurement. This is also the first measurement from the left visible, as a blue line, in figure 28.
4. In this step, the SDD was moved into the beam to a position where the beam hits the centre of the detector.
5. The power to the motorised goniometer was then switched off to eliminate any noise it generates, ensuring a noise-reduced measurement.
6. At this point, the data with the SDD was taken. At the same time, a measurement with the photodiode was performed, shown by the orange line in figure 28. Here, it is also visible that the SDD obstructs the beam from reaching the photodiode, resulting in a decreased current at the photodiode.
7. Once the SDD measurement is completed, the motors were switched back on and reinitialised.
8. While the motors were reinitialised, the beam valve was closed, and a background measurement for reference was taken using the photodiode. This measurement is coloured red in figure 28.
9. Afterward, the valve was reopened, and the detector was moved out of the beam.
10. Finally, the photodiode measured the unobstructed beam intensity again, completing the measurement sequence for one data point. The current at this step is shown by the green line in figure 28.

The data taken with the SDD are visualised as an energy spectrum, as seen in figure 29. In this spectrum, the unique features of the beam and the experimental setup are visible.

The most prominent peak in this energy spectrum is the beam's full energy peak (FEP), located at the configured energy. A backscattering tail can be seen on the

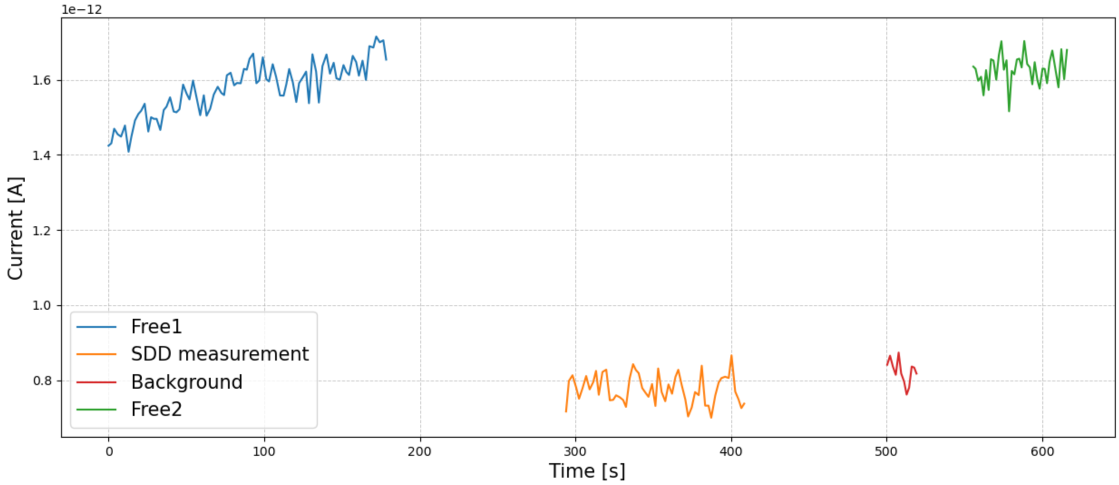

Figure 28: **Measurement sequence**
The first and last measurement was conducted with an unobstructed beam intensity, shown as blue and green lines, respectively. The orange line corresponds to the diode current during the SDD measurement, which also obstructed the beam from hitting the diode. The red line represents a background measurement with no beam. The here shown currents are for a beam energy of 10 keV.

low-energy side of this main peak. This feature results from photons being back-scattered and leaving the detector, only depositing a part of their energy in the main bulk of the SDD. A small peak is located in this low-energy tail. This feature represents the silicon escape peak resulting from electron ionisation. The first peak on the high-energy side of the main peak, along with the surrounding background, is

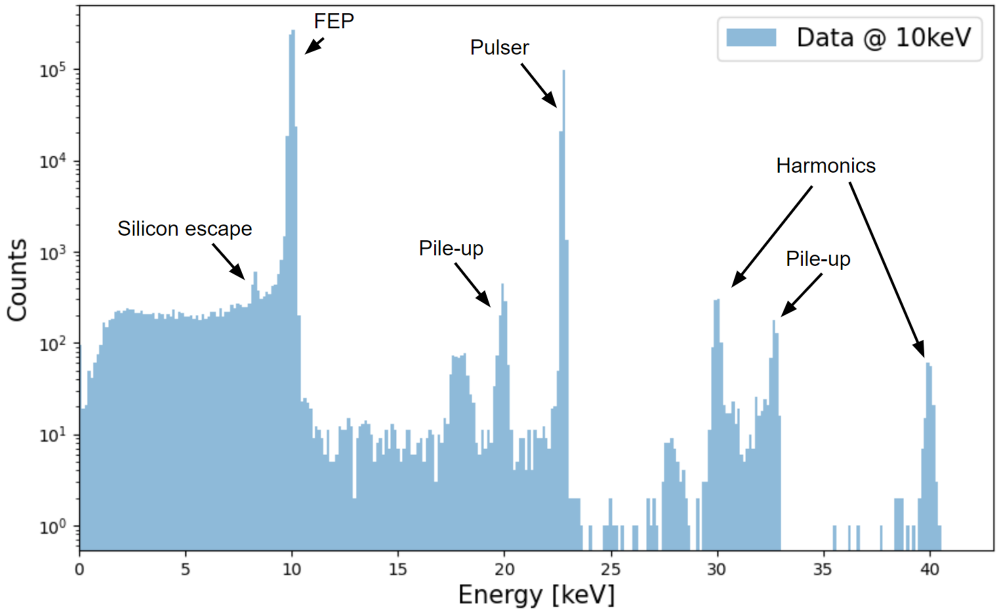

Figure 29: **SDD energy spectrum at** 10 keV **beam energy**
The full energy peak (FEP) is visible at 10 keV. Harmonics are visible at 3 and 4 times that energy. The silicon escape peak is visible at 8.3 keV, 1.7 keV below the main peak. The pulser was set at approximately 23 keV. Pile-up appears for both the main and pulser peaks.

caused by pile-up. This occurs when two or more events overlap partially or fully in time, resulting in a combined signal. The observed pile-up peak is produced when two events are detected almost simultaneously, leading to a higher-energy signal that appears as a single event. The second-highest peak in the energy spectrum is at approximately 23 keV and is from the pulser with a defined energy and rate. Since the Poisson distributed events can also overlap with the pulser event, a pulser pile-up peak occurs at an energy determined by the sum of the beam and pulser energy. Two more evident peaks are from the harmonics of the beam. They are located at three and four times the beam's energy.

4. Data Analysis

The analysis procedure to extract the absolute efficiency of the SDD from the data taken at the SOLEIL synchrotron is described in this chapter. This procedure was applied to 29 individual measurements carried out at 25 different beam energies in a range from 3 to 35 keV.

The analysis was divided into three steps:

1. **Beam rate determination**
   The beam rate is derived from the photodiode current. The photodiode in the back of the vacuum chamber, introduced in chapter 3.1.2, measures the total current induced by beam photons, which is used to estimate the beam rate. This is described in chapter 4.1.

2. **SDD rate determination**
   The SDD rate is derived from the energy spectra, using pulser events as rate calibration. This is described in chapter 4.2.

3. **Efficiency calculation**
   The efficiency is obtained as the ratio between the SDD and the beam rate. This ratio represents the energy-dependent absolute detection efficiency.

For illustration purposes, the individual steps of the data analysis are demonstrated using an example measurement at a beam energy of 10 keV.

4.1. Beam Rate Determination

The beam rate is adjusted by the angle of the second crystal of the monochromator as described in chapter 3.1.2. The photodiode is used to measure the beam current, which is then used to estimate the beam rate.

The output signal of the photodiode is a measured current that is recorded over the course of the measurement. This current represents the charge generated by the incident photon flux. Assuming a fully monochromatic beam, where all photons have the defined energy, allows for the calculation of the beam rate.

A challenge in determining the beam rate is that the rate of interest occurs during the SDD measurement when the SDD itself obstructs the beam. To address this, unobstructed photodiode measurements are taken before and after the SDD measurement, and the current at the time of the SDD measurement is estimated by interpolation.

When shutting off the beam, the photodiode measures a non-zero current. This background current is subtracted from the interpolated current as it does not originate from the beam intensity.

The beam current is calculated from both unobstructed diode measurements, named Free1 and Free2, respectively, minus the background current. Free1 and Free2 correspond to the first and last measurement of the data-taking procedure explained in chapter 3.4. The corresponding currents during both measurements are defined as I_{Free1} and I_{Free2} and corresponding time-stamps are t_{Free1} and t_{Free2}, respectively. The time of the SDD measurement is defined as t_{SDD}. These timestamps are the centre between the start and end of the corresponding measurement.

The Free1 and Free2 current measurements for the exemplary measurement at 10 keV beam energy can be seen in figure 30. The mean value and the corresponding statistical uncertainty are calculated for both measurements. The uncertainty is calculated using equation 14, representing the standard error of the mean. The values are (1.575 ± 0.008) pA for Free1 and (1.627 ± 0.006) pA for Free2 for the 10 keV measurement.

$$\sigma_{\mathrm{Free1/2}} = \frac{std(I_{\mathrm{Free1/2}})}{\sqrt{N_{\mathrm{Free1/2}}}} \tag{14}$$

Due to drifts in the beam intensity, the diode current I_{Beam} at the time of the SDD measurement is estimated by linear interpolation using:

$$I_{\mathrm{Beam}} = \left(\frac{I_{\mathrm{Free2}} - I_{\mathrm{Free1}}}{t_{\mathrm{Free2}} - t_{\mathrm{Free1}}} \cdot (t_{\mathrm{sdd}} - t_{\mathrm{Free1}}) \right) + I_{\mathrm{Free1}} \tag{15}$$

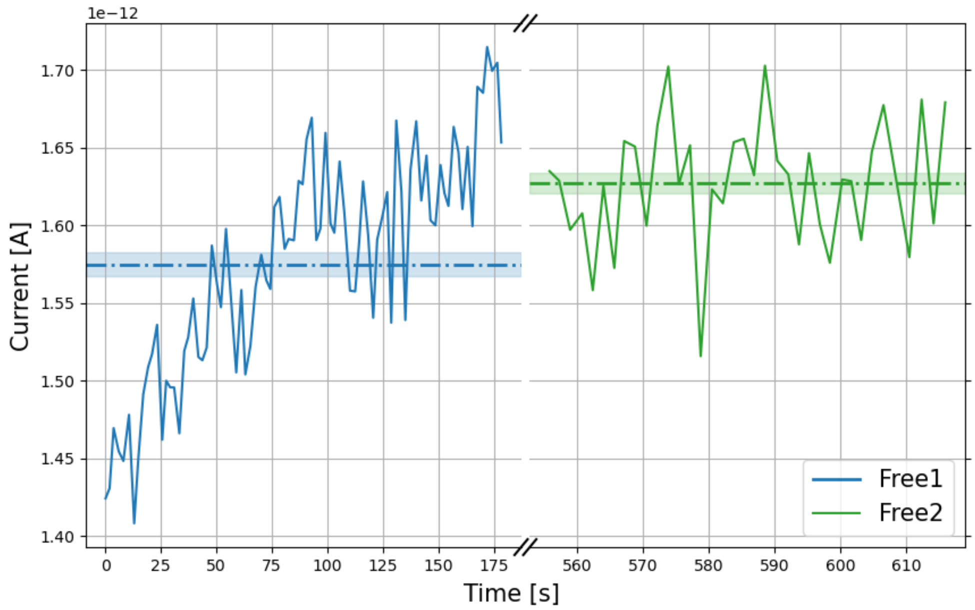

Figure 30: **Current during unobstructed measurement at** 10 keV
The first measurement (Free1) is shown as a blue line, and the second (Free2) is shown as a green line. The corresponding mean currents and uncertainties are indicated by the dotted lines.

An additional systematic uncertainty is introduced since the exact beam intensity path between Free1 and Free2 is not precisely known. The uncertainty corresponds to the maximum difference between the interpolated and individual values and is added in quadrature. For the measurement at 10 keV, this results in a beam current of

$$I_{\text{Beam}} = (1.599 \pm 0.005 \pm 0.028)\ \text{pA} = (1.599 \pm 0.028)\ \text{pA}. \tag{16}$$

The linear interpolation and the corresponding uncertainties for this measurement are shown in figure 31. For this data point, the interpolation uncertainty dominates the total uncertainty. This is not the case for all measurements carried out at different beam energies.

The next step in the beam rate determination is subtracting the background. The photodiode current with no beam was recorded during every measurement sequence. Figure 32 shows the background current consecutively across all measurements. The mean background is $I_{\text{bkgd}} = (0.8501 \pm 0.0049)$ pA and is indicated by a blue dotted line in figure 32.

This value is subtracted from the interpolated diode current. For the exemplary data point at a beam energy of 10 keV, this changes the beam current to $I_{\text{Beam}} = (0.749 \pm 0.028)$ pA. The beam current for all measurements is shown in figure 33. This figure also illustrates that the current was kept reasonably constant throughout

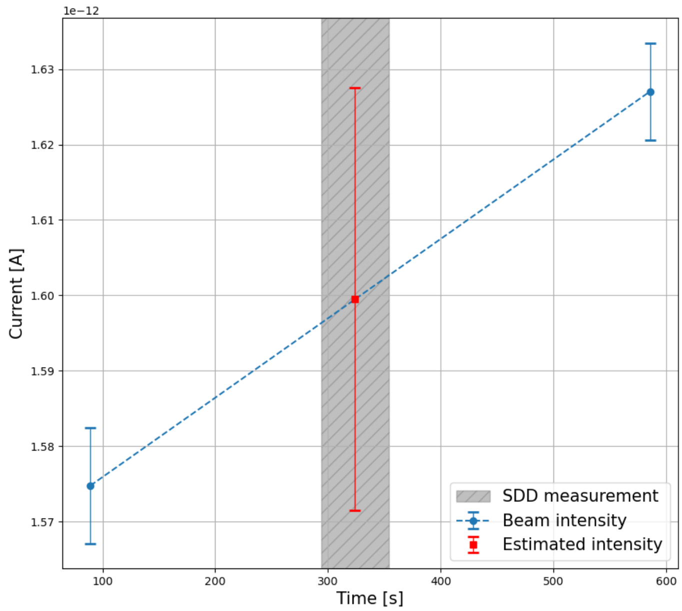

Figure 31: **Linear interpolation of the diode current at an energy of** 10 keV The linear interpolated value for the current during the SDD measurement is depicted as red data point. The error bars of the blue measurements represent the statistical uncertainty. The error bar of the red data point indicates the total uncertainty, including the systematic interpolation uncertainty.

all measurements. However, since the current had to be manually adjusted for each measurement, the beam intensity was slightly higher in the two measurements conducted at 9 keV beam energy. Even though these data points are slightly above the other measurements, this increased beam rate is not problematic for the SDD measurement.

The beam rate is calculated from this current for each measurement, based on the energy of the photons hitting the diode, using equation 17. This calculation assumes that the beam is perfectly monochromatic and all photons have the same energy. This assumption neglects harmonic contributions to the beam, due to higher-order Bragg-reflection in the monochromator, as described in chapter 3.1.2. The extent of this effect is discussed in chapter 4.3. The equation uses that current represents charge per second. Given that the mean energy to create free charge carriers and the energy of the incident photons are known, these values can be used to calculate the photon rate ω_{diode}.

$$\omega_{\text{diode}} = \frac{3.65 \cdot I}{0.98 \cdot e \cdot E} \cdot \left[1 - \exp\left(-\alpha\left(E\right) \cdot d\right)\right]^{-1} \tag{17}$$

I is the current measured by the photodiode. $R = \frac{0.98}{3.65}\frac{1}{\text{eV}}$ is the responsivity of the photodiode. The responsivity is the energy response for the incident light and

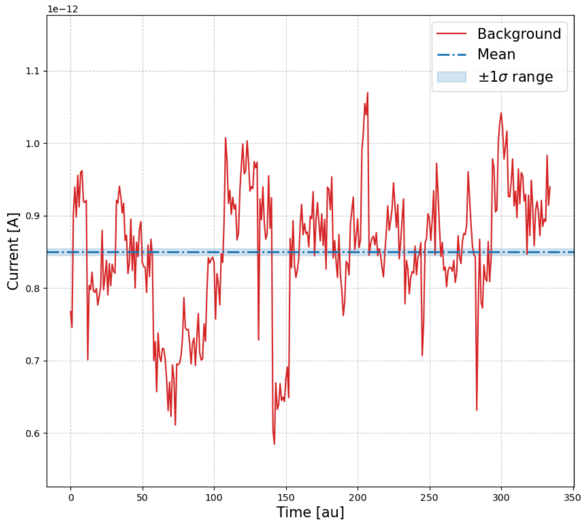

Figure 32: **Background current measured by the photodiode**
The current, measured without beam is depicted as red line. The mean value is indicated by the blue dotted line.

is composed of the average value for the electron-hole pair creation energy in silicon (3.65 eV) and a correction constant (0.98) given by the photodiode's manufacturer to account for the characteristics of the diode [85]. $e = 1.602 \times 10^{-19}$ C is the electron charge, and E is the energy of the incident photons. The factor $A(E) = 1 - exp\left(-\alpha(E) \cdot d\right)$ accounts for the absorption probability. The absorption

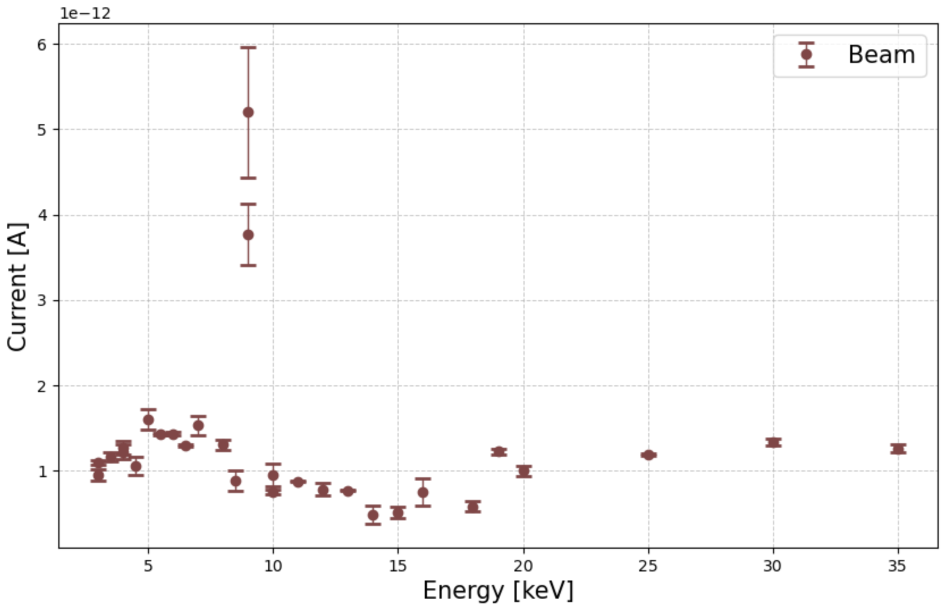

Figure 33: **Beam current for different energies**
The beam current was kept at a similar value for all measurements. Only at a beam energy of 9 keV a higher current was observed.

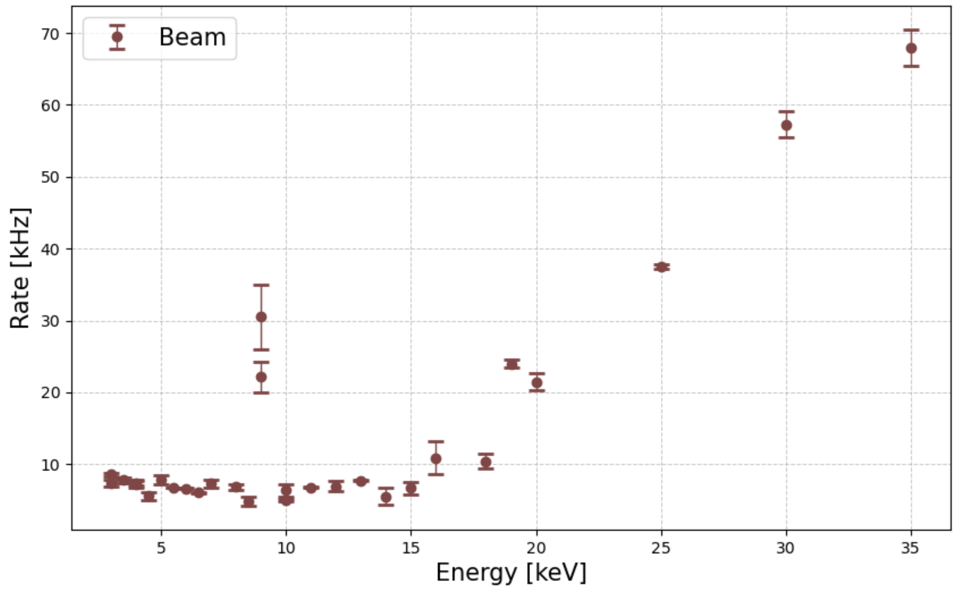

Figure 34: **Beam rate at different energies**
The beam rate is determined from the photodiode measurments. A correction for the decreasing absorption probability at higher energies is included.

coefficient α depends on the energy E of the incident photon and the properties of the detector material, here silicon. With the absorption coefficient $\alpha(E)$ of silicon, taken from [86], in combination with the photodiodes thickness $d = 55.5\,\mu\text{m}$, the absorption probability can be determined. The measurement of the SDD detection efficiency depends on this correction factor. A more accurate determination of the true beam rate could be obtained by using a photodiode with calibrated efficiency across the measured beam energies.

With equation 17 the beam rate for all measurements can be calculated. The resulting beam rate for each data point can be seen in figure 34. The uncertainty on the rate is determined by Gaussian error propagation. For the data point at 10 keV, this leads to a beam rate of $\omega_{\text{Beam}} = (5.03 \pm 0.19)$ kHz.

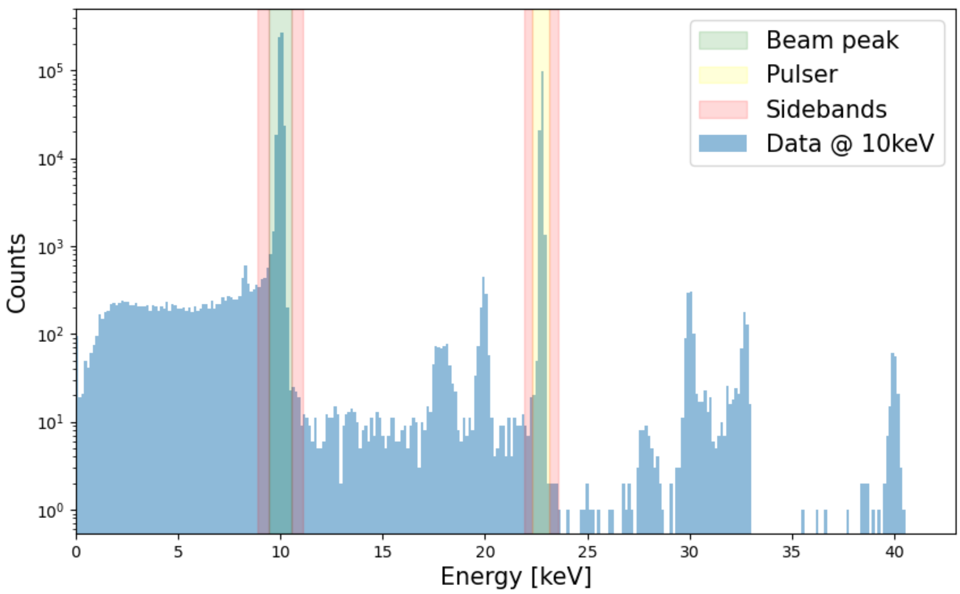

Figure 35: **Marked SDD energy spectrum at** 10 keV **beam energy**
The full energy peak at the main beam energy is marked in green. The pulser peak is marked yellow. The corresponding sidebands around both peaks are marked red.

4.2. SDD Rate Determination

The determination of the rate measured by the seven-pixel SDD varies considerably from the rate determination with the photodiode, elaborated in section 4.1. While the photodiode measures an integrated current for all incident photons, the SDD provides energy information on an event-by-event basis. In figure 35, the energy spectrum recorded at a beam energy of 10 keV is shown. The various features of this spectrum are explained in Chapter 3.4.

The rate determination is based on the two highest peaks in figure 35. They correspond to the full energy peak at the main beam energy and the peak from the pulse generator.

The reason for using the pulser is to avoid pile-up effects. The measurements are conducted at a Poisson distributed rate in the order of $\mathcal{O}(10)$kHz. At this rate pile-up, as well as the pile-up-related dead time of the DAQ system, can have a significant impact. For this reason, an artificial pulse was injected via the reset line just before each reset cycle, as described in Chapter 3.3.1. In this configuration, the additional pulses appear as regular events during the pulse processing and suffer the same pile-up effects as normal beam events. The pile-up effects occur for the pulse with the same probability as the beam. Since the pulser rate is known, it can be used as rate calibration.

The number of events in both peaks is obtained by integrating over a sufficiently wide window around each peak. Background events are taken into account by sideband subtraction, using sidebands with a width of $\frac{d}{2}$ next to the peak window of width d.

The typical number of events in the sideband is below 1% of the events in the peak region. For the 10 keV measurement, this results in 551535 ± 2056 full energy beam events, while 118691 ± 47 pulser events were recorded. The uncertainties take into account the statistical uncertainty of $\sqrt{N}$ in both the peak and sideband regions.

The beam rate is calculated using equation 18.

$$\omega_{\mathrm{FEP}} = \omega_{\mathrm{pulse}} \times \frac{N_{\mathrm{FEP}}}{N_{\mathrm{pulse}}} \cdot \kappa \tag{18}$$

Here, ω_{FEP} and ω_{pulse} are the full energy peak (FEP) and pulse rates, respectively. The uncertainty of this rate is determined by Gaussian error propagation. The correction factor is κ accounts for not recording data during the inhibit time described in chapter 3.3.1. By construction, the pulser events do not fall into the inhibit window, while beam events do. The duration of the inhibit is 5 μs every 1 ms, resulting in a correction factor of $\kappa = \frac{1}{0.95}$ on the number of events in the main peak. For 10 keV, this leads to a rate of (4.88 ± 0.02) kHz.

So far, this calculation relies on the events from the centre pixel of the seven-pixel SDD. Unfortunately, it is found that the beam shape is not completely circular and is not only hitting the central pixel. Especially at low energies, the beam is found to be horizontally elongated, depositing energy in the surrounding pixels. For visualisation purposes, a heat map of the beam's intensity in every pixel is calculated. The heatmaps for a beam energy of 3.5 and 18 keV are depicted in figure 36. At 3.5 keV, the beam has an elongated shape, spreading mostly into the left and right pixels, while at 18 keV, only the central pixel is hit. The number in the individual pixels is the fraction of events recorded with each corresponding pixel. In the following, the pixels will be referred to as described in figure 37.

In the exemplary measurement at 10 keV 89.3% of the beam hits the central pixel, as seen in figure 38. To accommodate this effect, the full rate analysis, which is done for the centre pixel, is also applied to the six surrounding pixels. This includes the peak identification, sideband subtraction, and error calculation. The corresponding results for the 10 keV data point can be seen in table 1.

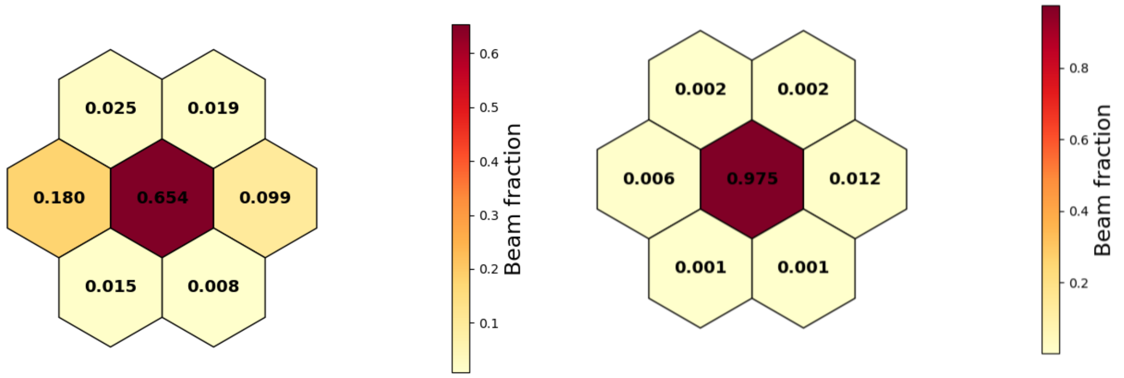

(a) Heatmap with a beam energy of $E = 3.5\,\mathrm{keV}$.

(b) Heatmap with a beam energy of $E = 18\,\mathrm{keV}$.

Figure 36: **Beam intensity heatmaps for 3.5 and 18 keV beam energy**
The heatmaps visualise the beam shape for two exemplary beam energies. the horizontally elongated beam shape at 3.5 keV is shown in the left panel. The desireable point-like beam is shown in the right panel. Each pixel's number represents the beam's fraction impacting that pixel.

Table 1: **Measured beam rate per pixel at a beam energy of** 10 keV
The individual rates and uncertainties for all seven pixels are shown.

Pixel	nw	ne	cw	cc
Rate [kHz]	0.075 ± 0.001	0.038 ± 0.001	0.238 ± 0.002	4.875 ± 0.016

Pixel	ce	sw	se
Rate [kHz]	0.155 ± 0.001	0.036 ± 0.001	0.012 ± 0.000

Ultimately, the seven individual rate calculations are combined into one rate representing the whole beam. This accommodation for the shape and spread of the beam introduces an additional error source, as it cannot be guaranteed that the entire beam is hitting the detection area of the SDD.

To include this error, an estimation of the amount of events not hitting the SDD

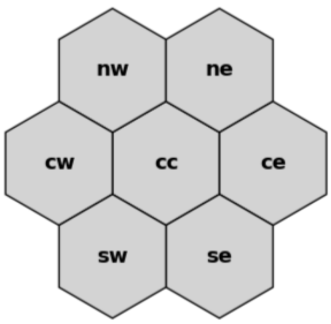

Figure 37: **Pixel naming method**
The seven pixels of the SDD are named corresponding to their position in the experimental setup.

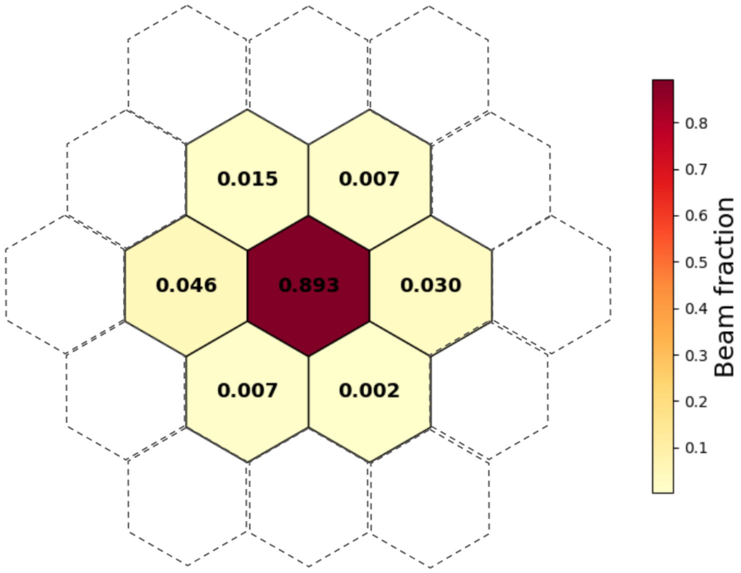

Figure 38: **Beam intensity heatmap for** 10 keV **beam energy**
This is a visualisation of the imaginary pixels surrounding the SDD, accounting for the uncertainty of the beam not only hitting the SDD's detection area. The heatmap in the centre shows the measured distribution of the beam's fraction in this measurement.

is performed. This estimation assumes 12 imaginary pixels surrounding the SDD's pixels. For each of these imaginary pixels, the potential fraction of the beam hitting that pixel is calculated. The contributions from all such pixels are then summed to estimate the total number of events that may be missing the detection area.

This value is then transformed into a rate, which is added as a systematic uncertainty to the rate measured by the SDD. A visualisation of this procedure applied on the 10 keV measurement is depicted in figure 38.

This results in a rate of $(5.428 \pm 0.016 \pm 0.027) = (5.428 \pm 0.031)$ kHz for the data point at a beam energy of 10 keV The same procedure is repeated for each data point in the measured range between 3 and 35 keV beam energy. The final measured rate at each beam energy can be seen in figure 39.

The systematic uncertainty dominates the uncertainty budget for measurements at beam energies below 9 keV. Above this energy, no significant rate was recorded in the outer pixels

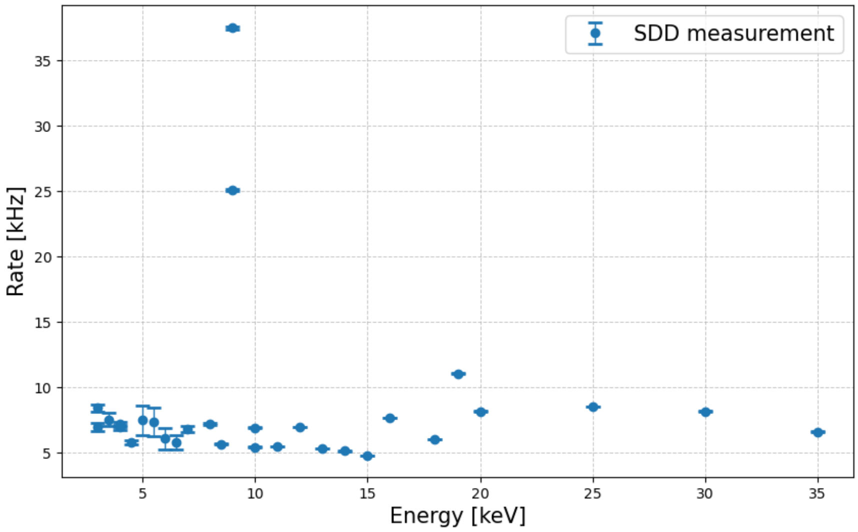

Figure 39: **Measured beam rate with the SDD**
The rate measured by the SDD for each beam energy with corresponding uncertainty is shown.

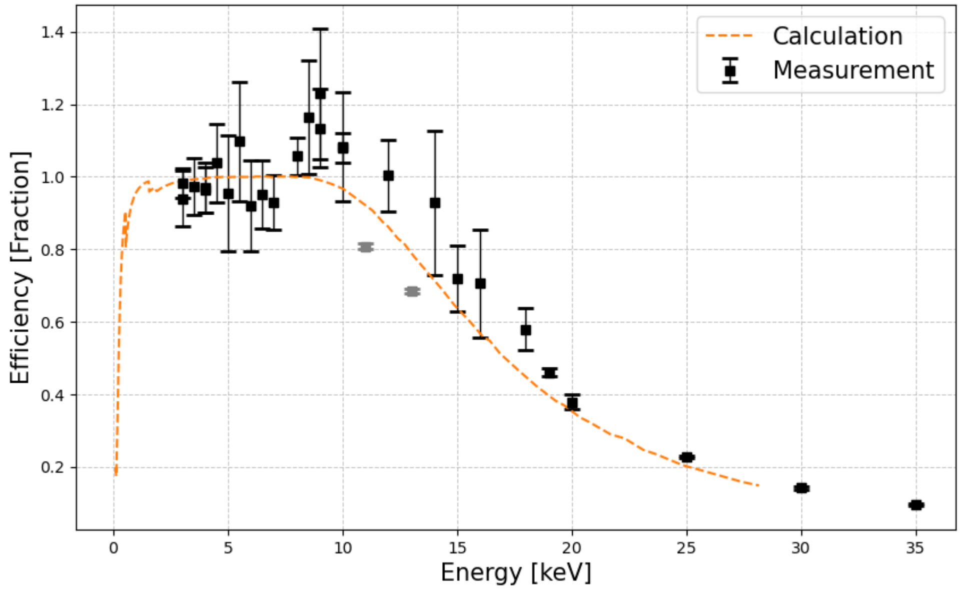

Figure 40: **Absolute SDD detection efficiency**
The measured absolute detection efficiency of the TAXO SDD is visualised as black squares. For reference, a calculated efficiency, taken from [56], is included as an orange dotted line.

4.3. Absolute Detection Efficiency of the TAXO SDD

The absolute detection efficiency of the TAXO SDD is determined as the ratio of the rate measured with the SDD and the beam rate estimated from the photodiode current, including corrections for the absorption coefficient of the photodiode. The efficiency ϵ is given by:

$$\epsilon = \frac{\omega_{\text{SDD}}}{\omega_{\text{Diode}}} \tag{19}$$

Here, ω_{SDD} is the SDD rate, and ω_{Diode} is the beam rate.

Using the diode rate values from chapter 4.1, the SDD rate values from chapter 4.2, and Gaussian error propagation to account for the uncertainties, the energy-dependent detection efficiency is determined as shown in figure 40.

For the exemplary data point at a beam energy of 10 keV, the detection efficiency of the SDD is determined to be $(108.32 \pm 4.14)\,\%$. This value is about 2σ above the value expected from calculations.

The measured detection efficiency follows the theoretical calculations. Considering that this is the first measurement of the TAXO SDDs efficiency, the results are consistent with the expectations. The main origin of the rather large errors at low energies is due to the unexpectedly large beam shape and fluctuations in the beam rate. At higher energies, the uncertainty from the photodiode on the beam rate dominates. The individual contributions to the uncertainty in the detection

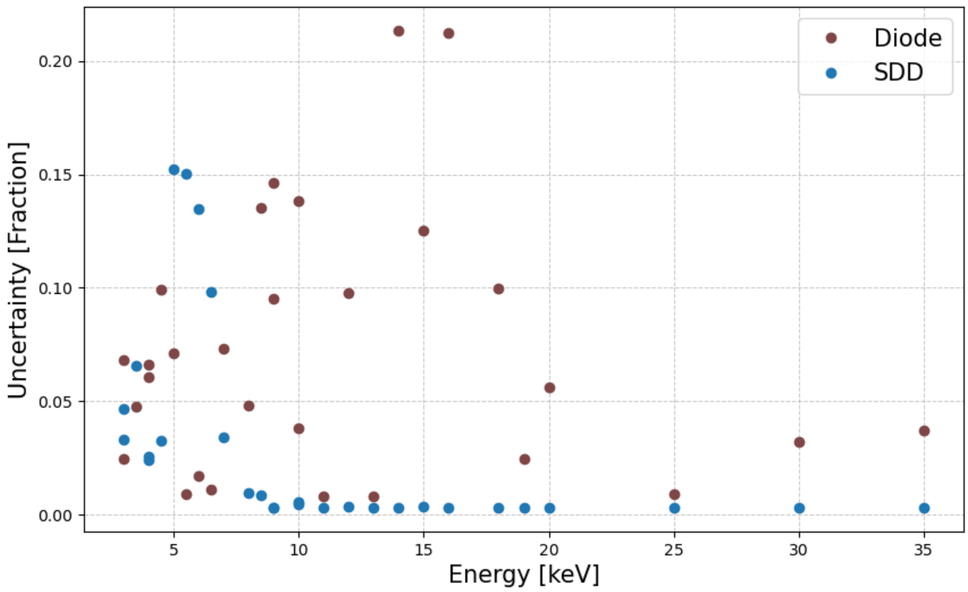

Figure 41: **Rate uncertainties**
The uncertainty from the SDD measurements is mostly relevant for lower energies and is depicted in blue. The dominant uncertainty for most data points arises from the beam determination with the photodiode, depicted in red.

efficiency can be seen in figure 41.

The efficiency obtained at 11 and 13 keV lies significantly below the neighbouring measurements. In the measurement at 11 keV, this is due to the pile-up of beam photons being located at the same energy as the pulser peak. This leads to an overestimation of the pulser counts with the current method, which is the reason for the underestimation of the efficiency. The reason for the lowered efficiency at 13 keV beam energy could not be resolved.

4.4. Beam Harmonics

A notable beam characteristic visible in the energy spectrum but neglected in this analysis is the contribution of harmonics to the beam intensity. This phenomenon is a side effect of the monochromator's working principle being based on Bragg-reflection, as mentioned in chapter 3.1.2.

The photodiode only measures an integrated current over all incident photons. In this case, the capability of the SDD to resolve the energy of the incident photons can be exploited. In order to determine the harmonics contribution to the photodiode current, the following steps were made.

The peaks associated with photons having three or four times the energy of the main beam energy are identified, and a rate for those photons in the beam is calculated.

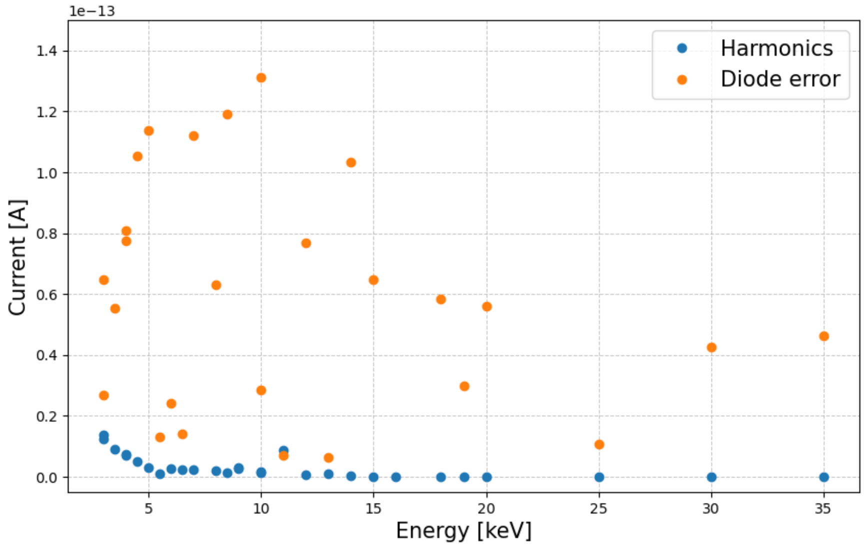

Figure 42: **Harmonic contribution**
the harmonic contribution to the measured photodiode current from the monochromatic beam is depicted as blue dots. For reference, the value of the uncertainty at each energy is shown as orange dots.

This is done similarly to the SDD rate determination described in chapter 4.2. This rate is then corrected by taking the absorption probability of the SDD into account. The reverse process described in chapter 4.1 is applied to calculate the diode current contribution from the photon rate generated by harmonics.

The resulting maximum contribution is approximately 10^{-2} pA, two orders of magnitude lower than the measured current ($\mathcal{O}\,(\mathrm{pA})$). The contribution of harmonics decreases with increasing beam energy as the absorption in the thin photodiode gets very unlikely. The harmonic contribution to the beam current, compared to the size of the respective uncertainty, is shown in figure 42. The harmonics in the beam intensity were disregarded for this analysis due to the minimal magnitude of the contribution.

5. Conclusion and Outlook

In this thesis, I measured the absolute X-ray detection efficiency of the TAXO SDD, currently under development for the BabyIAXO experiment. This efficiency was first experimentally determined for the TAXO SDD by this thesis while only being theoretically determined before. The excelent detection efficiency is one of the most important properties of a detector for being capable of measuring the X-ray photons in an axion searching experiment.

The measurements were conducted at the hard X-ray branch of the Metrology beamline at the SOLEIL synchrotron. The detection efficiency was measured in an energy range between 3 and 35 keV beam energy. The absolute detection efficiency of the SDD was found to be close to 100% for photon energies below 10 keV. Above that energy, the detection efficiency decreases, as expected from calculations. The near-perfect detection efficiency for single-digit keV X-rays and the decreasing detection efficiency at higher energy X-rays match the theoretical predictions. The measured data points closely follow the theoretical curve, validating the expected efficiency performance of the SDD.

During the stay at the SOLEIL synchrotron, we could not take any data at the low X-ray branch of the Metrology beamline for energies between 0.3 keV and 2 keV due to electrical noise issues. The SDD detection efficiency below the measured 3 keV is also relevant for IAXO, as most of the axion flux from axion-to-electron couplings is in this range. It would be valuable to resolve this issue and take data in this energy range to probe the SDD's detection efficiency for the full range of solar axions. This could be done with future measurements at the SOLEIL facility or at other X-ray sources in the corresponding energy range.

The reference beam rate was determined via measurements with a photodiode and corresponding theory-based correction factors. The precision of the final result would be improved by using a better-known photodiode with a properly calibrated efficiency curve to compare the TAXO SDD's performance against.

Several beam-related effects may have introduced uncertainties to the result. In the measurements, only a fraction of the synchrotron beam's potential rate was utilized to better resolve individual events in the SDD. The beamline setup, however, is optimized for significantly higher beam rates. These effects could be removed by taking data at another X-ray source or by increasing the data-taking time significantly.

Although there is potential to expand and improve further measurements, the result of this work was the first experimental validation of the TAXO SDD's excellent detection efficiency. This brings the TAXO project closer to being incorporated into the promising IAXO helioscope experiment.

List of Figures

1 Illustration of the axion potential 4
2 Feynman diagram of The Primakoff effect 5
3 Axion parameter space exclusions 8
4 Working principle of a haloscope 9
5 Working principle of Light-Shining-through-a-Wall (LSW) experiments 10
6 Solar axion flux spectra 12
7 Structure of an axion helioscope 12
8 Conceptual IAXO design 13
9 Conceptual design of the IAXO magnet bore system 14
10 Projected axion parameter space for IAXO 16
11 Conceptual design for BabyIAXO 17
12 Concept of a reverse biased p-n junction 23
13 Schematic diagram of an SDD 24
14 TRISTAN seven-pixel SDD 24
15 Theoretical SDD detection efficiency 25
16 SOLEIL synchrotron facility 26
17 SOLEIL synchrotron beamlines 27
18 Beamline distribution across different energy ranges 28
19 Vacuum chamber for the hard X-ray branch of the Metrology beamline 30
20 Peltier element concept 31
21 Holder for SDD with included cooling and heat drain system 32
22 Signal processing chain and experimental setup 33
23 CAEN data acquisition card 34
24 Components for data acquisition 35
25 Sample waveform analysis 36
26 Positioning of the SDD 38
27 Beam intensity scan 39
28 Measurement sequence 41
29 SDD energy spectrum at 10 keV beam energy 41
30 Current during unobstructed measurement at 10 keV 45
31 Linear interpolation of the diode current at an energy of 10 keV . . . 46
32 Background current measured by the photodiode 47
33 Beam current for different energies 47
34 Beam rate at different energies 48
35 Marked SDD energy spectrum at 10 keV beam energy 49
36 Beam intensity heatmaps for 3.5 and 18 keV beam energy 51
37 Pixel naming method 51
38 Beam intensity heatmap for 10 keV beam energy 52

39 Measured beam rate with the SDD 53
40 Absolute SDD detection efficiency 54
41 Rate uncertainties 55
42 Harmonic contribution 56

List of Tables

1 Measured beam rate per pixel at a beam energy of 10 keV 51

Acronyms

SDD	Silicon drift detector
PCB	Printed circuit board
TRISTAN	Tritium spectrometer with silicon drift detector array
MMC	Metallic magnetic calorimeters
DAQ	Data acquisition system
nJFET	n-channel junction field effect transistor
IAXO	International axion observatory
QCD	Quantum chromodynamics
EDM	Electric dipole moment
KSVZ	Kim-Shifman-Vainshtein-Zakharov
DFSZ	Dine-Fischler-Srednicki-Zhitnitskii
WISP	Weakly interacting slim particle
DM	Dark matter
WIMP	Weakly interacting massive particle
LSW	Light-shining-through-a-wall
ADMX	Axion dark matter experiment
HPL	High power laser
ALPS	Any light particle search
OSQAR	Optical search for QED vacuum birefringence, axions, and photon regeneration
CAST	CERN axion solar telescope
MST	Medium-sized telescope
CTA	Cherenkov telescope array
XMM	X-ray multi-mirror mission
Micromegas	Micromesh gaseous structure
TPC	Time projection chamber
TAXO	Tritium for IAXO
LINAC	Linear accelerator
VLS-PGM	Varied line spacing plane grating monochromator
DCM	Double crystal monochromator
TC	Thermocouple
wf	Waveform
FEP	Full energy peak

References

[1] L. Wolfenstein, "Violation of CP invariance and the possibility of very weak interactions," *Phys. Rev. Lett.*, vol. 13, pp. 562–564, Nov 1964.

[2] W. Marciano and H. Pagels, "Quantum chromodynamics," *Physics Reports*, vol. 36, no. 3, pp. 137–276, 1978.

[3] J. E. Kim and G. Carosi, "Axions and the strong *cp* problem," *Rev. Mod. Phys.*, vol. 82, pp. 557–601, Mar 2010.

[4] M. B. Gavela, M. Ibe, P. Quilez, and T. T. Yanagida, "Automatic peccei–quinn symmetry," *The European Physical Journal C*, vol. 79, no. 6, p. 542, 2019.

[5] H. Leutwyler, "On the vacuum angle in QCD," tech. rep., CERN, Geneva, 1983.

[6] D. J. and E. Marsh, "Axions and alps: a very short introduction," *arXiv: High Energy Physics - Phenomenology*, 2017.

[7] C. Abel *et al.*, "Measurement of the permanent electric dipole moment of the neutron," *Phys. Rev. Lett.*, vol. 124, p. 081803, Feb 2020.

[8] I. G. Irastorza, "An introduction to axions and their detection," *SciPost Phys. Lect. Notes*, p. 45, 2022.

[9] R. D. Peccei and H. R. Quinn, "CP conservation in the presence of pseudoparticles," *Phys. Rev. Lett.*, vol. 38, pp. 1440–1443, Jun 1977.

[10] R. D. Peccei and H. R. Quinn, "Constraints imposed by CP conservation in the presence of pseudoparticles," *Phys. Rev. D*, vol. 16, pp. 1791–1797, Sep 1977.

[11] H. Davoudiasl and M. Schnubel, "Bringing peccei-quinn mechanism down to earth," 06 2024.

[12] F. Björkeroth, E. J. Chun, and S. F. King, "Accidental peccei–quinn symmetry from discrete flavour symmetry and pati–salam," *Physics Letters B*, vol. 777, pp. 428–434, 2018.

[13] J. Goldstone, "Field theories with ≪ superconductor ≫ solutions," *Il Nuovo Cimento (1955-1965)*, vol. 19, no. 1, pp. 154–164, 1961.

[14] S. Weinberg, "A new light boson?," *Phys. Rev. Lett.*, vol. 40, pp. 223–226, Jan 1978.

[15] F. Wilczek, "Problem of strong p and t invariance in the presence of instantons," *Phys. Rev. Lett.*, vol. 40, pp. 279–282, Jan 1978.

[16] F. D'Eramo, "Axions in the early universe," *SciPost Physics Proceedings*, 07 2023.

[17] R. Bernabei and C. Tao, *The Dark Side of the Universe.* WORLD SCIENTIFIC, 1994.

[18] H. Primakoff, "Photo-production of neutral mesons in nuclear electric fields and the mean life of the neutral meson," *Phys. Rev.*, vol. 81, pp. 899–899, Mar 1951.

[19] P. Sikivie, "Experimental tests of the "invisible" axion," *Phys. Rev. Lett.*, vol. 51, pp. 1415–1417, Oct 1983.

[20] G. G. Raffelt, "Astrophysical axion bounds diminished by screening effects," *Phys. Rev. D*, vol. 33, pp. 897–909, Feb 1986.

[21] G. G. Raffelt, "Astrophysical methods to constrain axions and other novel particle phenomena," *Physics Reports*, vol. 198, no. 1, pp. 1–113, 1990.

[22] K. Altenmüller *et al.*, "A new upper limit on the axion-photon coupling with an extended CAST run with a Xe-based Micromegas detector," tech. rep., 2024.

[23] S. Andriamonje *et al. Journal of Cosmology and Astroparticle Physics*, vol. 2007, p. 010, apr 2007.

[24] H. S. Røising, B. Fraser, S. M. Griffin, S. Bandyopadhyay, A. Mahabir, S.-W. Cheong, and A. V. Balatsky, "Axion-matter coupling in multiferroics," *Phys. Rev. Res.*, vol. 3, p. 033236, Sep 2021.

[25] J. Ruz, J. Vogel, and M. Pivovaroff, "Recent constraints on axion-photon and axion-electron coupling with the cast experiment," *Physics Procedia*, vol. 61, pp. 153–156, 2015. 13th International Conference on Topics in Astroparticle and Underground Physics, TAUP 2013.

[26] K. Barth *et al.*, "Cast constraints on the axion-electron coupling," *Journal of Cosmology and Astroparticle Physics*, vol. 2013, p. 010, may 2013.

[27] G. Raffelt, "Limits on a *cp*-violating scalar axion-nucleon interaction," *Phys. Rev. D*, vol. 86, p. 015001, Jul 2012.

[28] A. Ringwald, "Searching for axions and alps from string theory," *Journal of Physics: Conference Series*, vol. 485, p. 012013, mar 2014.

[29] P. W. Graham and others., "Experimental searches for the axion and axion-like particles," *Annual Review of Nuclear and Particle Science*, vol. 65, no. Volume 65, 2015, pp. 485–514, 2015.

[30] I. G. Irastorza and J. Redondo, "New experimental approaches in the search for axion-like particles," *Progress in Particle and Nuclear Physics*, vol. 102, pp. 89–159, 2018.

[31] V. C. Rubin and J. Ford, W. Kent, "Rotation of the Andromeda Nebula from a Spectroscopic Survey of Emission Regions," *apj*, vol. 159, p. 379, Feb. 1970.

[32] K. Garrett and G. Dūda, "Dark matter: A primer," *Advances in Astronomy*, vol. 2011, no. 1, p. 968283, 2011.

[33] C. O'Hare, "cajohare/axionlimits: Axionlimits." `https://cajohare.github.io/AxionLimits/`, July 2020.

[34] O. Kwon *et al.*, "First results from an axion haloscope at capp around 10.7 μeV," *Phys. Rev. Lett.*, vol. 126, p. 191802, May 2021.

[35] C. Boutan *et al.*, "Axion dark matter experiment: Run 1a analysis details," *Phys. Rev. D*, vol. 109, p. 012009, Jan 2024.

[36] K. Van Bibber *et al.*, "Proposed experiment to produce and detect light pseudoscalars," *Phys. Rev. Lett.*, vol. 59, pp. 759–762, Aug 1987.

[37] P. Arias *et al.*, "Optimizing light-shining-through-a-wall experiments for axion and other weakly interacting slim particle searches," *Phys. Rev. D*, vol. 82, p. 115018, Dec 2010.

[38] P. Pugnat *et al.*, "Search for weakly interacting sub-ev particles with the osqar laser-based experiment: results and perspectives," *The European Physical Journal C*, vol. 74, no. 8, p. 3027, 2014.

[39] M. Diaz Ortiz *et al.*, "Design of the alps ii optical system," *Physics of the Dark Universe*, vol. 35, p. 100968, 2022.

[40] "Physics: Not a wisp of evidence," *Nature*, vol. 465, no. 7296, p. 271, 2010.

[41] U. Oberlack and P. Sissol, eds., *Axions WIMPs and WISPs: Proceedings, 9th Patras workshop, PATRAS 2013, Mainz, Germany, June 23-28, 2013*, (Hamburg), 9th Patras Workshop on Axions, WIMPs and WISPs, Mainz (Germany), 24 Jun 2013 - 28 Jun 2013, DESY, Jun 2013.

[42] M. Maroudas, ed., *13th "Patras" Workshop on Axions, WIMPs and WISPs, PATRAS 2017*, DESY-PROC, (Hamburg), 13th Patras Workshop on Axions, WIMPs and WISPs, Thessaloniki (Greece), 15 May 2017 - 19 May 2017, Verlag Deutsches Elektronen-Synchrotron, May 2018. ISSN 1435-8077; C17-05-15.4.

[43] I. Irastorza *et al.*, "The International Axion Observatory IAXO. Letter of Intent to the CERN SPS committee," 8 2013.

[44] I. A. Observatory, "Diagram of the international axion observatory." `https://iaxo.desy.de/`, 2024. Accessed: 2024-10-07.

[45] R. Kotthaus *et al.*, "The x-ray telescope of the cast experiment," 2005.

[46] D. D. Heuchel, "3d-model of the BabyIAXO design concept." Email to the author, 2024. Received: 2024-10-07.

[47] A. Abeln *et al.*, "Conceptual design of BabyIAXO, the intermediate stage towards the international axion observatory," *Journal of High Energy Physics*, vol. 2021, May 2021.

[48] I. Irastorza *et al.*, "Towards a new generation axion helioscope," *Journal of Cosmology and Astroparticle Physics*, vol. 2011, p. 013–013, June 2011.

[49] V. A. et al., "New cast limit on the axion–photon interaction," *Nature Physics*, vol. 13, pp. 584–590, Jun 2017.

[50] Y. Stockman *et al.*, "Xmm flight mirror module with reflection grating assembly and x-ray baffle testing," *Proceedings of SPIE - The International Society for Optical Engineering*, vol. 3445, 11 1998.

[51] T. Dafni and J. Galan, "Digging into axion physics with (baby)iaxo," 12 2021.

[52] K. Altenmüller *et al.*, "X-ray detectors for the BabyIAXO solar axion search," *Nuclear Inst. and Methods in Physics Research, A*, vol. 1048, p. 167913, 2023.

[53] C. Ligtenberg *et al.*, "Performance of a GridPix detector based on the Timepix3 chip," *Nuclear Instruments and Methods in Physics Research Section A*, vol. 908, pp. 18–23, 2018.

[54] V. Anastassopoulos *et al.*, "Improved search for solar chameleons with a GridPix detector at CAST," *Journal of Cosmology and Astroparticle Physics*, vol. 2019, p. 032, 01 2019.

[55] D. Unger *et al.*, "High-resolution for IAXO: MMC-based x-ray detectors," *Journal of Instrumentation*, vol. 16, p. P06006, 06 2021.

[56] D. Schlosser *et al.*, "Expanding the detection efficiency of silicon drift detectors," *Nuclear Instruments and Methods in Physics Research Section A: Accelerators, Spectrometers, Detectors and Associated Equipment*, vol. 624, no. 2, pp. 270–276, 2010. New Developments in Radiation Detectors.

[57] T. Eggert *et al.*, "Analysis of background events in silicon drift detectors," *Nuclear Instruments and Methods in Physics Research Section A: Accelerators, Spectrometers, Detectors and Associated Equipment*, vol. 512, no. 1, pp. 257–

264, 2003. Proceedings of the 9th European Symposium on Semiconductor Detectors: New Developments on Radiation Detectors.

[58] L. Schönfeld, "Cosmic background studies of a silicon drift detector setup for the IAXO experiment," master's thesis, Technical University of Munich, Munich, Germany, April 2024.

[59] T. group, "Conceptual design report: Katrin with tristan modules," 2022. Karlsruhe Tritium Neutrino (KATRIN) experiment.

[60] KATRIN Collaboration, "Katrin design report 2004," tech. rep., Forschungszentrum Jülich, 2005. 51.54.01; LK 01.

[61] F. Hartmann, *The Evolution of Silicon Detector Technology*, vol. 275 of *Springer Tracts in Modern Physics*. Springer, 2024.

[62] T. Knežević, L. K. Nanver, and T. Suligoj, "Silicon drift detectors with the drift field induced by pureb-coated trenches," *Photonics*, vol. 3, no. 4, 2016.

[63] L. Strüder *et al.*, "Silicon drift detector – the key to new experiments," *Sci Nat*, vol. 85, pp. 539–543, 1998.

[64] P. Lechner *et al.*, "Silicon drift detectors for high count rate x-ray spectroscopy at room temperature," *Nuclear Instruments and Methods in Physics Research Section A: Accelerators, Spectrometers, Detectors and Associated Equipment*, vol. 458, no. 1, pp. 281–287, 2001.

[65] B. Wuenschek *et al.*, "Temperature dependencies of the energy and time resolution of silicon drift detectors," 03 2011.

[66] K. Altenmüller *et al.*, "Background discrimination with a Micromegas detector prototype and veto system for BabyIAXO," *Frontiers in Physics*, vol. 12, 2024.

[67] A. Nava *et al.*, "A geant4-based model for the tristan detector," *Journal of Physics: Conference Series*, vol. 2156, p. 012177, dec 2021.

[68] D. Spreng, "Electron backscattering on silicon drift detectors and its impact on a sterile neutrino search with KATRIN," Master's thesis, Technical University of Munich, Max-Planck-Institute for Physics, Department of Physics, March 2023.

[69] S. Mertens *et al.*, "Characterization of silicon drift detectors with electrons for the tristan project," *Journal of Physics G: Nuclear and Particle Physics*, vol. 48, p. 015008, dec 2020.

[70] P. Trigilio *et al.*, "Ettore: a 12-channel front-end asic for sdds with integrated jfet," in *2018 IEEE Nuclear Science Symposium and Medical Imaging Conference Proceedings (NSS/MIC)*, pp. 1–4, 2018.

[71] C. Wiesinger, "Dataset on GEANT4 detection efficiency simulation." Received on October 07, 2024. Personal communication.

[72] Synchrotron SOLEIL, "Position along the storage ring," 2024.

[73] J. Susini *et al.*, "A brief introduction to the synchrotron SOLEIL and its upgrade programme," *The European Physical Journal Plus*, vol. 139, p. 80, January 2024.

[74] S. Synchrotron, "Parameters of the accelerators and storage ring," 2024. Accessed: 2024-09-08.

[75] M. Idir *et al.*, "Metrology and Tests beamline at SOLEIL Design and first results," *AIP Conference Proceedings*, vol. 1234, pp. 485–488, 06 2010.

[76] T. T. Prasad, M. H. Modi, and G. S. Lodha, "Optical Design of VLS-PGM Soft X-Ray Beamline on Indus-2," *AIP Conference Proceedings*, vol. 1234, pp. 375–378, 06 2010.

[77] Z. Hou, "Ray tracing study for a detuned nondispersed double crystal monochromator," *Review of Scientific Instruments*, vol. 76, p. 013305, 12 2004.

[78] A. Morawiec, *Basic Aspects of Crystal Diffraction*, pp. 79–121. Cham: Springer International Publishing, 2022.

[79] J. Pérez–Aparicio, R. Palma, and R. Taylor, "Finite element analysis and material sensitivity of peltier thermoelectric cells coolers," *International Journal of Heat and Mass Transfer*, vol. 55, no. 4, pp. 1363–1374, 2012.

[80] V. A. Drebushchak, "The peltier effect," *Journal of Thermal Analysis and Calorimetry*, vol. 91, no. 1, pp. 311–315, 2008.

[81] Z. Slanina, M. Uhlik, and V. Sladecek, "Cooling device with peltier element for medical applications," *IFAC-PapersOnLine*, vol. 51, no. 6, pp. 54–59, 2018. 15th IFAC Conference on Programmable Devices and Embedded Systems PDeS 2018.

[82] S. Xiaoyong *et al.*, "Experimental analysis of high temperature peek materials on 3d printing test," in *2017 9th International Conference on Measuring Technology and Mechatronics Automation (ICMTMA)*, pp. 13–16, 2017.

[83] CAEN, "Caen v1782 octal digital multi-channel analyzer," 2024. Accessed: 2024-09-10.

[84] P. Mercère and P. Da Silva, “Metrology and test beamline,” *SOLEIL*, 2024. Beamline dedicated to the metrology and characterization of X-ray optical components and detectors.

[85] A. T. Ltd, *AXUV Series Absolute UV Silicon Photodiodes*. AP Technologies Ltd, The Coach House, Watery Lane, Bath, BA2 1RL, UK, 2020. Accessed: 2024-10-02.

[86] C. Chantler *et al.*, “Detailed tabulation of atomic form factors, photoelectric absorption and scattering cross section, and mass attenuation coefficients for z= 1-92 from e = 1-10 ev to e = 0.4-1.0 mev,” 2005. National Institute of Standards and Technology (NIST), Accessed on September 30, 2024, Last updated January 2005.

Acknowledgements

I would like to thank all the people who supported me during the time of my master thesis. I am especially grateful for the assistance and guidance of the following people:

Prof. Dr. Susanne Mertens - I want to thank You for giving me the opportunity to work within the E47 group and do such fascinating research for my master thesis with the IAXO collaboration. I am grateful for Your support during all that time. Through You, I was introduced to the scientific community.

Dr. Christoph Wiesinger - I want to thank You for being the best supervisor I could ask for. You always took the time to help me with any problems I had. I admire Your calm and confident approach to the problems before, during, and after the experiment.

Daniel Siegmann - I want to thank You for Your readiness to help with any problem, even when You were not involved in it. I especially want to thank You for joining the measurements at SOLEIL. This would not have worked as well as it did without You.

Paco and Claude - Thank You for the support during the whole project. I am grateful for Your assistance at SOLEIL and for answering all my questions afterwards.

Lucinda Schönfeld and Juan Pablo Ulloa Betete - Thank You for being such awesome colleagues and friends. Especially at the beginning, You had the patience to explain to me how everything worked and where to find what. Because of You, I am so happy to be part of the TAXO group.

Office colleagues - I want to thank all of You for all the help and all the enjoyable conversations, making the work there memorable but also productive.

E47 group - Thank You all for incorporating me so quickly in this group, where everyone was ready to help me, even with the smallest problems.

My Parents - I want to thank You for enabling me to study what I am really interested in and supporting me the whole time.

Family and friends - I want to thank You for Your support and love all this time.